

Design of a liquid ^3He target

Magnus Sjöström

**Master's thesis
LTH, MAX-lab
June 2004**

Abstract

A liquid ^4He cryostat at the tagged-photon facility at MAX-lab, Lund, has been modified into a prototype cryostat capable of ^3He condensation through pumping on a ^4He bath. This bath is refilled through a fixed flow impedance capillary connected to a ^4He reservoir. In the redesign work, a thermal analysis of the original cryostat as well as the developed prototype was made using MATLAB and the finite-element method based software FEMLAB. This thermal analysis, along with tests, indicated heat leaks into the reservoir of the order of 15 mW. Heat leaks into the pumped ^4He bath could not be determined.

The prototype reached a temperature of approx. 2 K for about 10 minutes. The primary failing of the cryostat prototype was identified to be the flow impedance, which was too large.

The FEMLAB simulation models developed for the thermal analysis include radiative and conduction heat transfer. Lack of accurate data of the properties of the materials for low temperatures coupled with approximations regarding radiative heat transfer limited the accuracy of the simulations.

Sammanfattning

En flytande ^4He kryostat vid 'tagged-photon' anläggningen hos MAX-lab, Lund, har modifierats för klara av kondensering av ^3He genom pumpning på en ^4He volym. Denna volym återfylls från en ^4He reservoar via en kapillär med fixt flödesmotstånd. I modifieringsarbetet gjordes en analys av både den ursprungliga kryostatens och den framtagna prototypens termiska prestanda med hjälp av MATLAB och FEMLAB, baserat på finita element metoden. Denna termiska analys, tillsammans med mätningar, indikerade en värmeläcka på 15 mW in i ^4He reservoaren. Värmeläckan in i den pumpade ^4He volymen kunde inte fastställas.

Prototypen nådde en lägsta temperatur på ca 2 K under 10 minuter. Prototypens primära problem var kapillärens flödesimpedans, vilken befanns vara för stor.

De FEMLAB modeller som utvecklats för den termiska analysen stöder värmetransport via strålning och ledning. En brist på information om materialegenskaper vid låga temperaturer begränsade, tillsammans med approximativa värmestrålningsberäkningar, noggrannheten i simuleringarna.

Acknowledgements

By no means was this thesis project completed solely by the author; several people assisted with not only valuable advice and ideas, but also worked on the cryosystem. I would like to thank Kurt Hansen in particular, who as my acting supervisor at MAX-lab assisted me with ideas and valuable discussions on practically every part of the project, and also put in a lot of effort to rebuild the old cryostat in order to get measurements.

I'd also like to thank my supervisor Lennart Isaksson at the Nuclear Physics department of Lund University for his help regarding beam physics and the requirements on the cryostat target. Both he and Bent Schröder also have my thanks for their valuable input regarding the report. Nils-Erik Persson of the MAX-lab workshop receives thanks for his superb and speedy workmanship – getting the LPC leak tight even for superfluid He II is no mean achievement.

A special thank you goes to Dr. Hartmut Dutz of the Polarised target group in Bonn, for taking the time to discuss the preliminary cryostat design and the very helpful advice he gave regarding heat leaks and cryostat performance.

Further, I'd like to thank the Photonuclear research group in Lund for their advice and interest in the project as well as the Royal Physiographic Society in Lund for their support.

I'd also like to thank Martin Karlsson, Per Lilja, Magnus Lundin and Erik Ljungbertz for interesting lunch discussions both related and unrelated to the project.

Table of contents

1	BACKGROUND	2
2	CRYOSTAT DESIGN	4
2.1	THE ORIGINAL CRYOSYSTEM	4
2.2	DESIRED CHARACTERISTICS	7
2.3	THE REDESIGNED CRYOSYSTEM.....	8
3	THEORY	12
3.1	FLOW IMPEDANCE	12
3.2	HEAT CONDUCTION	14
3.2.1	<i>Bulk heat conduction</i>	14
3.2.2	<i>Contact resistance</i>	15
3.3	RADIATIVE HEAT TRANSFER	15
3.3.1	<i>Emissivity temperature variations</i>	18
3.3.2	<i>Multi-layered insulation</i>	19
3.4	CONVECTION AND ACCOMMODATION HEAT TRANSFER.....	19
3.5	BEAM HEAT TRANSFER	20
4	FEMLAB MODEL	22
4.1	DEFINITIONS.....	22
4.2	SHORT DESCRIPTION OF FEMLAB	22
4.3	GEOMETRY MODEL	23
4.3.1	<i>Model optimisations</i>	23
4.3.2	<i>Björn Nilsson experiment</i>	24
4.3.3	<i>³He condensation experiment</i>	25
4.4	PHYSICS MODEL.....	26
4.4.1	<i>Björn Nilsson experiment</i>	27
4.4.2	<i>³He condensation experiment</i>	31
4.5	SIMULATION.....	35
4.5.1	<i>Mesh settings</i>	35
4.5.2	<i>Solver options</i>	35
4.5.3	<i>Initial values</i>	36
5	EXPERIMENTS	38
5.1	EQUIPMENT	38
5.1.1	<i>Temperature sensors</i>	38
5.1.2	<i>Pressure sensors</i>	40
5.1.3	<i>Evacuation system</i>	40
5.1.4	<i>Level probe</i>	41
5.2	EXPERIMENTAL SET-UP	41
5.2.1	<i>Preliminary set-up</i>	41
5.2.2	<i>³He condensation set-up</i>	44
6	EXPERIMENT RESULTS	46
6.1	³ HE CONDENSATION	46
7	SIMULATION ANALYSIS	50
7.1	BJÖRN NILSSON'S EXPERIMENT	50
7.1.1	<i>Simulation results</i>	50
7.1.2	<i>Simulation validity</i>	53
7.2	³ HE CONDENSATION EXPERIMENT	55
7.2.1	<i>Simulation results</i>	55
7.2.2	<i>Simulation validity</i>	57
8	CONCLUSIONS	60

APPENDIX A: SIMULATION LIST.....	62
A.1 ORIGINAL CRYOSYSTEM SIMULATIONS	62
A.2 ³ He CONDENSATION CRYOSYSTEM SIMULATIONS.....	63
APPENDIX B: MATERIAL PROPERTIES.....	64
B.1 MATERIAL DESCRIPTIONS.....	64
<i>B.1.1 Liquid ⁴He</i>	64
<i>B.1.2 MLI and aluminised mylar</i>	64
<i>B.1.3 Aluminium</i>	65
<i>B.1.4 Copper</i>	65
<i>B.1.5 Stainless steel</i>	66
<i>B.1.6 Lead</i>	66
B.2 MATLAB PROPERTY FUNCTIONS	67
B.3 MATERIAL DATA SOURCES	68
APPENDIX C: CALIBRATION CHARTS.....	70
LIST OF ABBREVIATIONS.....	74
LIST OF VARIABLES.....	76
LITERATURE LIST	78
LIST OF REFERENCES	80

1 Background

Recent theoretical models predicting the binding energies of nuclei using only nucleon-nucleon forces have been successful, but only to a point. Deviations between the calculated binding energies and the observed are considerable for light nuclei; the predicted binding energies are consistently lower than the observed. If three-nucleon forces are taken into account by using theoretical models such as Tucson-Melbourne and Urbana IX [1], predictions that are far more accurate can be made.

In order to study three-nucleon forces more closely, suitable study objects have to be found. One of the more ideal is the ^3He nucleus, where the photodisintegration reactions $^3\text{He}(\gamma, d)p$ and $^3\text{He}(\gamma, pp)n$ might be studied using the photon beam facility at MAX-lab. Data from these reactions could then possibly allow refinement of current three-nucleon force models.

In order to be able to measure the reactions at MAX-lab however, a liquid ^3He target is necessary due to the economical and technical difficulties of constructing a less dense gas phase target simply because of the size it would have to be. As liquid ^3He is not commercially available, the design of a cryosystem allowing liquefaction of ^3He would be required. For this, temperatures lower than 3,2K are needed at atmospheric pressures, something the pre-existing cryosystems at MAX-lab could not achieve.

It was therefore judged expedient to begin modifications of a liquid ^4He cryostat previously utilised at MAX-lab for experiments by B. Nilsson [2], T. Glebe [3] and S. Proff [4]. Beside modifications geared toward achieving lower temperatures than 4,2K, improving the cryostat performance in terms of cryogenic liquid consumption was deemed a priority since the basic design of the ^4He cryostat could not be altered to allow continuous refilling of liquid ^4He . Hence, the cryostat will need periodic refilling, during which time no measurements can be taken and precious beam time will be lost. Extending the time between refills through minimising heat leaks would then greatly improve the economy of any future measurements on a condensed ^3He target.

This project was therefore initiated with the aim to study the heat leaks in the previous cryostat and to aid in the development of a liquid ^3He cryostat prototype. To achieve this, the stated objectives prior to initiation were twofold:

1. To develop a simulation environment of the cryostat system at MAX-lab.
2. To build a cryostat prototype allowing condensation of ^3He .

2 Cryostat design

2.1 The original cryosystem

During previous low temperature experiments such as measurements of the ${}^4\text{He}(\gamma, n)$ reaction, the photonuclear research group in Lund built a cryosystem.

In preparation for measurements on ${}^3\text{He}$, it was decided that rather than to build or purchase a new system the old would be modified to support the liquefaction of ${}^3\text{He}$. A cursory description of the old cryostat is therefore in order.

The cryosystem as it was used during an experiment with a liquid ${}^4\text{He}$ photon beam target is displayed in Figure 2.1. The large, cylindrical ${}^4\text{He}$ reservoir in the centre is shielded from its hot surroundings by first an isolation vacuum jacket to minimise heat conduction, convection and accommodation. It is then shielded from thermal radiation along most of its length by a liquid N_2 jacket dewar. To conserve liquid N_2 , this jacket dewar is then isolated from the outer walls of the cryostat by the same isolation vacuum.

Thermal radiation from the 300 K room temperature surroundings is prevented from entering the reservoir through the top end by polished Cu plates and multiple layers of NRC-2 aluminised mylar acting as radiation shields, as shown in Figure 2.2. The target is a simple extension of the reservoir, consisting of a kapton plastic foil cylinder with a steel plate bottom. Since it is plastic, the highest Z of the kapton foil component atoms is that of C and thus allows beam entry with minimal disruption of the beam.

In order to protect the target from thermal radiation, for which the target was unshielded, a Cu frame was bolted to the liquid N_2 jacket dewar to act as a radiation shield. The Cu frame consisted of plates of variable thickness (0,9 – 3,0 mm) upon which five Cu plates 0,3 mm thick were fastened with metal straps as shown in Figure 2.3. Further, three layers of 0,03 mm thick aluminium foil as well as multilayer insulation (MLI) shielding consisting of five layers of NRC-2 super insulation were wrapped around it. Some small slits were made in the shielding to allow measurements of the target helium density [5]. Any heat transferred to the Cu frame would then be conducted to the liquid N_2 dewar, which acted as a thermal sink.

The original cryosystem required periodic refilling of cryogenic liquids, most often liquid ${}^4\text{He}$, during which time the beam had to be shut off. The usual time between refills was 24 h.

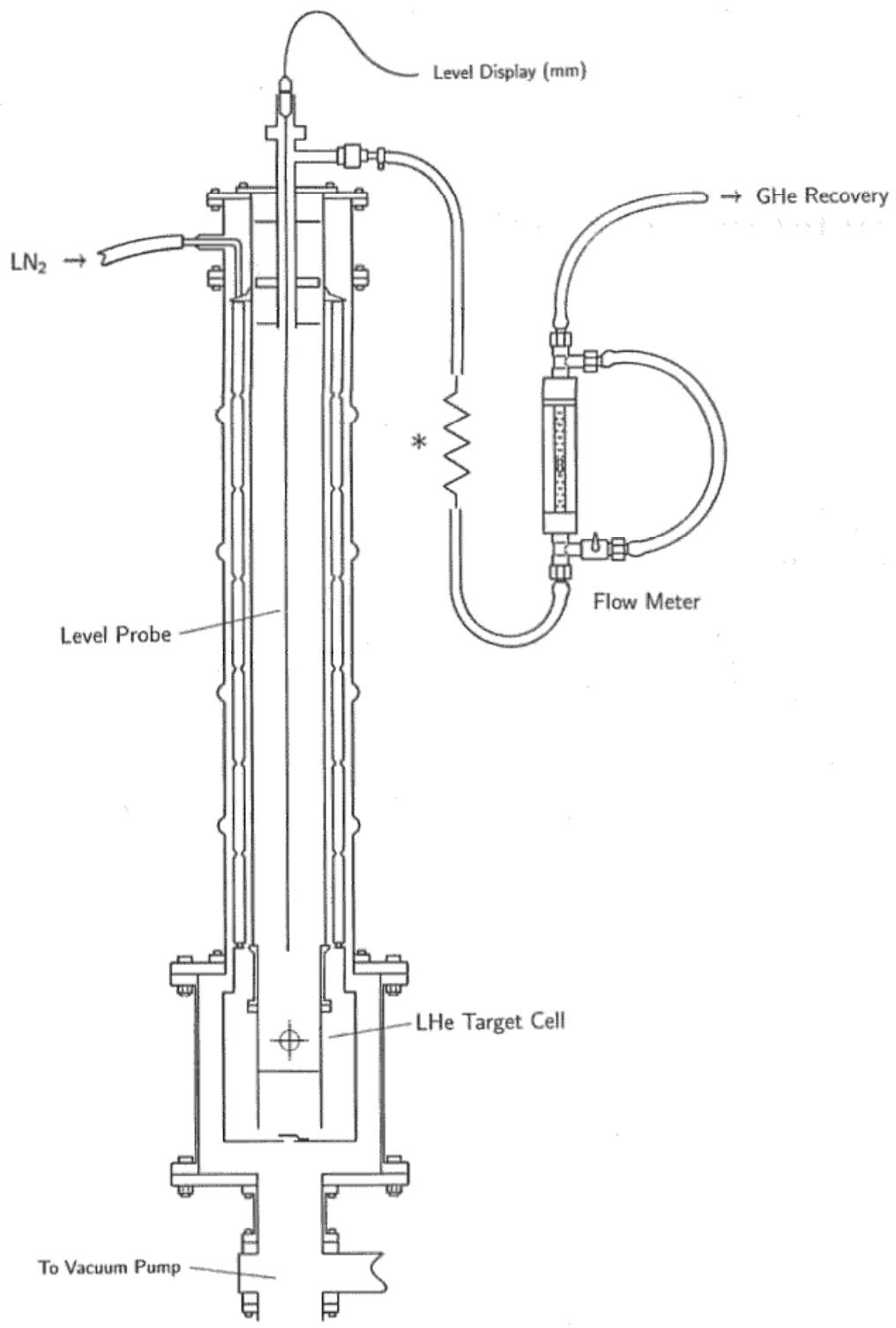


Figure 2.1: The cryostat system used for measurements of the ${}^4\text{He}(\gamma, n)$ reaction. Marked in the figure are the superconducting level probe, the gas flow meter and a heat exchanger (marked with ‘*’) to heat up the cold ${}^4\text{He}$ vapour before the flow meter. The liquid ${}^4\text{He}$ target cell, made out of Kapton foil, is marked close to the bottom of the cryostat.



Figure 2.2: The radiation shield at the top of the reservoir, seen from two different angles. Between the Cu plates several layers of aluminised mylar have been inserted in an attempt to decrease the amount of thermal radiation that will penetrate from the topmost steel flange which will be at 300 K during operation. Three thin-walled steel tubes penetrate the mylar layers and support both them and the three Cu plates. The middle Cu plate has a slightly larger radius than the other two, as well as contact surfaces intended to thermally anchor the plate to the reservoir wall, which at that height has a direct connection to the liquid N₂ jacket dewar.



Figure 2.3: The liquid N₂ anchored Cu radiation shield used in the ⁴He(γ,n) experiment. To the left, the basic Cu frame is shown. To the right, a photograph of the radiation shield with the additional five Cu plates attached.

2.2 Desired characteristics

The cryostat is intended only to provide a condensed ^3He beam target for experiments at MAX-lab. As liquid ^3He is not a staple commodity, the cryostat will be required to perform the condensation of ^3He gas. This will require lower temperatures than 3,2 K, assuming the condensation will take place at atmospheric pressure. The exceedingly high price, 140 € excl. VAT per 25 dm³ of ^3He gas at atmospheric pressure [6], also makes the need for recycling as much gas as possible a priority.

In order for the target measurements to produce good data, the target density has to be known very well. Further, the measurements will take several days in order to accumulate sufficient data that random fluctuations are minimised.

Due to this, problems arise of both a technical and economical nature. The technical ones mainly derive from the necessary refills of cryogenic liquids, a characteristic of the cryosystem that unfortunately could not be altered. These refills will disturb the thermal equilibrium established in the cryostat during measurements. Since the ^3He density is directly related to the temperature as shown in Figure 2.4, this will in turn cause fluctuations in the ^3He density and result in down-time during which no meaningful measurements can be taken until thermal equilibrium has been re-established. One way to avoid such a scenario is minimisation of the liquid helium consumption. This directly corresponds to a minimisation of heat leaks. Another possible way is to keep the thermal transients, introduced to the cryosystem by refilling it, as short in time as possible.

Separate from the thermal transients caused by refilling the cryostat, there will be unavoidable temperature fluctuations even after the transients caused by a refill have died out. These can be caused by acoustic noise and vibrations, or from electrical heating of level meters in the cryostat. Since these will be unavoidable, the temperature of the ^3He target will have to be measured continuously in order to know the correct ^3He target density.

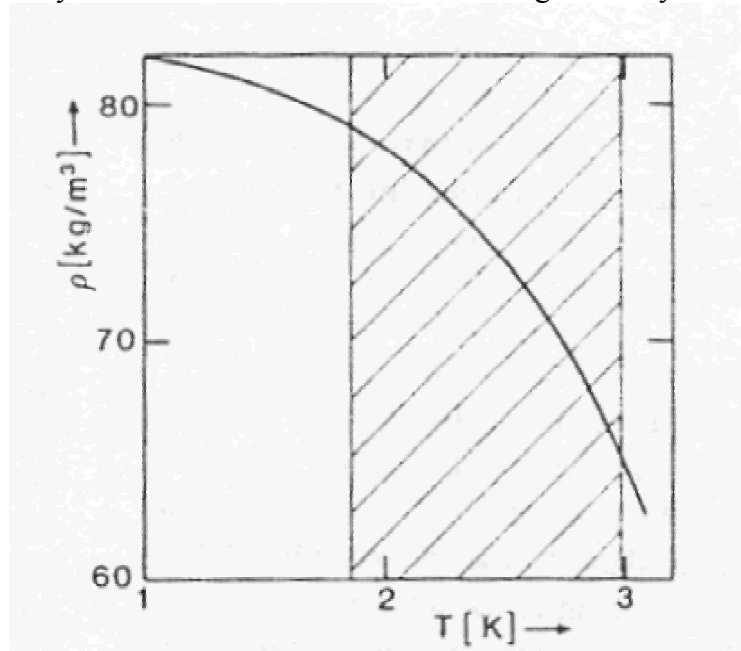


Figure 2.4: The density of liquid ^3He as a function of temperature [7].

The economical problems are due to the fact that beam time is expensive. This provides motivation for solving the technical problems stated above, since the option of having the cryostat only to supply a condensed ^3He target with a stable temperature for, say, 10% of the time would be far too expensive.

2.3 The redesigned cryosystem

In order to accommodate the requirements stated in section 2.2, several alterations were made to the pre-existing cryosystem. This work took place over several months and a prototype was ready only a few weeks before the end of the thesis project. In the course of this work, design discussions with Dr. H. Dutz of the Polarised target group at Universität Bonn were conducted. As Dr. Dutz has extensive experience working with cryogenic targets, his advice was invaluable.

In order to provide temperatures lower than 3,2 K for the condensation process, a low-pressure chamber (henceforth referred to as LPC) was attached below the liquid ^4He reservoir. Liquid ^4He from the reservoir would continuously fill the LPC, in which the lower pressure would lower the boiling point of the fluid, and thus the LPC temperature. ^3He gas would then be made to condense through exchanging heat with the LPC. After the discussions with Dr. H. Dutz [8], a Cu capillary tube coil was placed inside the LPC to act as the heat exchanger, which can be seen in Figure 2.5.

The replacement of the evaporated ^4He in the LPC was accomplished with a capillary tube connecting the reservoir with the ^4He . The four major considerations in the design of the capillary were; allowing a pre-cooling of the 4,215 K liquid ^4He before it entered the LPC, restrict the flow of ^4He so as to roughly match the evaporation rate in the LPC, avoid the blocking of the capillary by having frozen air or other impurities sucked in, and to avoid a large conduction heat leak between the reservoir and the LPC.

Other ways to accomplish refilling of the LPC were considered, such as mounting the LPC inside the reservoir and utilise thin pores in the LPC wall for refilling. This would however have introduced far too large heat leaks between the reservoir and the LPC, and the idea was thus discarded.

The pre-cooling was deemed necessary should the LPC temperature drop below the λ -point of ^4He , which lies at 2,17 K and below which the ^4He turns superfluid (see section B.1.1). As observed by Raccanelli, Reichertz & Kreysa [9], injection of He I into a He II bath would lead to the generation of vibration noise that in turn might generate heat. While the intent is to run the cryostat at a temperature slightly above the λ -point, in order to avoid the problems with He II super-leaks through the LPC solder connections and weldings, it is conceivable that it will have to be run below the λ -point in order to guarantee a stable enough ^3He target density. As shown in Figure 2.4, the slope of the ^3He $\rho(T)$ function is less steep at lower temperatures, thus reducing the impact of any temperature fluctuations in the target.

The flow impedance is necessary to balance carefully, since should it be too large the LPC will quickly empty and thus heat up. An LPC temperature of 2,3 K require an LPC pressure of 6,7 kPa; thus a pressure difference of roughly 94 kPa will be present over the capillary. Should the flow impedance be too small, this pressure difference would cause a column of ^4He to rise up the LPC evacuation tube to the point where the heat leaks from the tube supports would start to quickly evaporate the liquid. Unfortunately, the optimal flow impedance proved exceedingly difficult to determine. This was due to several factors; the most important being turbulent flows in combination with large temperature dependencies of liquid ^4He properties such as viscosity, density and heat capacity. In addition, the possibilities of superfluid back-flow below the λ -point due to the temperature gradient in the fluid (see B.1.1), along with the property changes of the liquid ^4He below this temperature, made a simulation too difficult for the author to attempt. The conclusion was made at an early stage that the optimal design solution would include a valve to allow for regulation of the flow. The Polarised Target Group at Bonn University has made needle valves for cryogenic liquids, with which they have had positive experiences according to Dr. H. Dutz. However, no needle valve

was acquired for the cryosystem prototype at MAX-lab, due to considerable restraints on the project time as well as workshop capabilities. Beside the difficulties inherent in manufacturing the needle valve itself, the modifications of the cryostat necessary to utilise it would not have been trivial. Therefore, a fixed flow impedance of the ‘wire-in-the-capillary’ type was used. Instead of using a thinner capillary tube, a large capillary was blocked up with a steel wire to reduce the cross-section area and increase the inside surface area (see section 3.1). Unfortunately, the resulting flow impedance is very hard to predict accurately if this method is used.

An alternative way to make a fixed flow-impedance would have been to pack the capillary with sintered powder. According to Gauthier and Varoquaux [10], this method would make it possible to manufacture desired flow impedances more accurately. However, the desired impedance was not known beforehand, as no simulations of the heat leaks were ready at the time. Thus, the prime advantage of the more complex method of packing the capillary with sintered powder would have been irrelevant.

A potential problem with a the capillary tube is that residual gases in the reservoir may, upon filling the cryostat with liquid ^4He , solidify and accumulate at the bottom, close to the capillary entrance. Should these be sucked into the capillary, they may block it completely. This was prevented by the attachment of a sintered filter to the reservoir end of the capillary, as can be seen in Figure 2.5.



Figure 2.5: Picture showing the reservoir bottom flange. The outer wall of the pumping tube can be seen coming in from the right and the LPC, with both ends of the Cu capillary acting as heat exchanger between the LPC and the ^3He gas visible sticking out from the LPC, is partly obscured in the left side of the picture by the flange. The steel capillary piercing the flange is the refill capillary, upon which a sintered filter has been fitted to prevent solidified gases and other particles from entering the capillary.

To extend the time between refills, different heat leaks into both the ^4He reservoir and the LPC had to be identified and minimised. In the case of the reservoir, the previous experiment by B. Nilsson had shown that the vast majority of the heat entering the liquid ^4He did so by radiative heat transfer through the Kapton foil target cell. Conduction heat leaks along the reservoir walls as well as radiative heat transport from the liquid N_2 jacket dewar to the reservoir were shown to be minimal in comparison. As the ^3He condensation cryosystem would replace the Kapton foil target with a steel flange this heat leak would be almost entirely removed. Efforts were thus concentrated on the LPC.

To minimise radiative heat transfer between the radiation shield anchored thermally to the liquid N_2 jacket dewar and the LPC, a second radiation shield was bolted to the bottom of the reservoir. This radiation shield was made out of a length of uniform copper pipe 1,35 mm thick and 78 mm in diameter. The outside was polished in order to reduce emissivity. Though this significantly decreased the radiative heat leak into the LPC, it also introduced a conduction heat leak into the reservoir as any heat absorbed in the radiation shield would be conducted to the reservoir. Due to the far lower emissivity of the radiation shield as compared to the steel and kapton target utilised by B. Nilsson, the amount of heat transferred to the reservoir would nevertheless be smaller in total.

No changes were made to the MLI shielding covering the radiation shield bolted to the liquid N_2 jacket dewar. It was judged desirable to replace the entire radiation shield, in order to eliminate material uncertainties, thermal contact resistances and grief during cryostat assembly. It was however assigned low priority due to the minor performance improvement expected and difficulties deciding on a new design and at the end time did not allow any changes.

Conduction heat leaks into the LPC were easily identified to conduction along the pumping pipe supporting the LPC beneath the reservoir, the capillary refilling the evaporated ^4He and the ^3He gas line leading ^3He gas into the heat exchanger inside the LPC.

Minimising the heat leak from the pumping pipe was done through making the pumping pipe double-walled for a length of 0,9 m from the bottom of the reservoir, with the walls separated by the cryostat isolation vacuum. This made the distance to the closest hot spot, the pumping pipe wall joints, 0,93 m. The alternative solution with a single-walled pumping pipe would have resulted in a far larger heat leak since it would have put only 3 cm pipe between the 4,2K reservoir and the LPC.

In order to minimise the conduction heat leak along the capillary to the LPC, the capillary was made out of steel tubing ($\text{Ø}3\text{mm}$, 0,5mm wall thickness) the first 2 cm of the way between the reservoir and the LPC. Then Cu tubing ($\text{Ø}2\text{mm}$, 0,8mm wall thickness) was used. This allowed for an efficient capillary-LPC heat exchange without introducing the large thermal conductance of Cu between the reservoir and the LPC. The connection between the Cu and steel tubing was made with flux-coated silver solder from Böhler-Thyssen. The Cu tubing had to be inserted about half a cm into the steel tubing to prevent solder from blocking the capillary. The $\text{Ø}0,78\text{mm}$ wire inside the capillary was made out of steel all the way through, since this did not affect the efficiency of the heat exchange with the LPC.

The ^3He gas line was made of steel tubing ($\text{Ø}2\text{mm}$, 0,8mm wall thickness). It entered the cryostat close to the top between the liquid N_2 jacket dewar and the ^4He reservoir. Care was taken to thermally anchor the line to the jacket dewar close to the top and then allow it to go down between the jacket dewar and the reservoir; nonetheless sporadic thermal contact between the jacket dewar and the capillary on the way down towards the target area was deemed highly likely due to deformations of the gas line. A Swage-lock coupling was used to connect the gas line with the LPC before entering through the ^4He anchored radiation shield.

During the final stage of the thesis project, an attempt to condensate ^3He was made. While no target was available, a small dummy volume was mounted on the heat exchanger.

3 Theory

3.1 Flow impedance

When initially designing the capillary connecting the ^4He reservoir with the LPC, a major concern is the magnitude of the ^4He flow. Should it be too small, pumping will cause the LPC to empty and no cooling effect will be obtained. Should it be too large, pumping will cause a liquid ^4He pillar to rise inside the pumping tube up to hot areas – causing a vastly increased rate of boil-off and hence a decrease in the time between reservoir refills. Even should the pillar be too short to reach hot areas, the shorter distance between these hot spots and the liquid surface will cause the amount of heat transferred by thermal conduction along the pumping tube's inner wall to increase.

To illustrate the importance of substantial flow impedance between the reservoir and the LPC, consider the following. At a pressure of 6730 Pa the boiling point of liquid ^4He is 2,3 K. Should the capillary not offer any flow resistance at all, i.e. the pressure at the capillary's LPC entry point is 101 kPa, the resulting pressure difference would be able to support a liquid ^4He column 65 meters high.

Many cryostats utilise needle valves to allow regulation of the flow impedance. The use of a fixed impedance capillary requires knowledge about the conditions under which it will be used, such as the pressure difference between the end points, the fluid viscosity, et.c.

While there are standardised methods that can be used to determine wanted pipe or capillary dimensions in order to obtain a certain flow, these have been developed for temperatures around and above 300 K. At these temperatures, the properties of a fluid usually do not change greatly with temperature. At cryogenic temperatures, with liquid helium close to its boiling point, additional difficulties arise that vastly complicate the calculations.

Firstly, the properties of liquid helium vary considerably with pressure and temperature. Along the 101 kPa isobar, the viscosity increases with roughly 17% as the temperature drops from 4,2 K to 3,3 K, after which it again decreases. The density is strongly temperature dependent as well as a slightly dependent on the pressure.

Secondly, unless the temperature along a capillary drops quicker than the liquid helium boiling point does, which is affected by the declining pressure in the capillary, phase changes inside the capillary will occur. This would produce helium gas inside the capillary which, given a downwards liquid flow, will flow counter to the liquid. This would then impede the liquid flow in an unpredictable manner.

Thirdly, should at any time the liquid helium undergo a phase transition into the superfluid state the viscosity will no longer be easily described by conventional theory. Further, the possibility of superfluid back-flow will arise, where a temperature gradient will cause liquid helium to flow in the opposite direction.

These additional concerns, along with the traditional difficulties of dealing with turbulent flows, result in a very complicated system. While it may be possible to simulate the system in FEMLAB for different capillary diameters, no ready application mode allows the simulation of a flow at once both non-isothermal and turbulent. It will therefore require the use of a FEMLAB PDE mode and knowledge of the partial differential equations describing such a flow. In addition, knowledge of how the liquid helium properties vary with both temperature and pressure will be required.

Different empirical methods for correctly designing desired liquid ^4He flow impedances were therefore examined early in the project. Information was unfortunately scarce. In addition, project time considerations imposed harsh limits. Simulations and calculations on the size of the heat leaks were not finished at the point when a capillary design had to be decided upon.

Previous measurements by DeLong, Symko & Wheatly [11] provided liquid ${}^4\text{He}$ molar flow rates for three different capillaries characterised by their impedance factor Z , measured for helium gas at 300 K. The definition of the flow impedance, or impedance factor, Z is

$$Z = \frac{\Delta p}{\eta \cdot \dot{V}},$$

where Δp is the pressure difference across the channel, \dot{V} the volume rate of laminar flow of gas and η the gas viscosity. The three different impedances had been achieved through putting wires with different dimensions inside the capillaries in order to restrict the flow.

The estimated molar flow rate through the capillary required to replace evaporated liquid ${}^4\text{He}$ in the LPC was found to closely agree with the molar flow rates measured by DeLong et al., thereby providing likely values for capillary flow impedance.

A different method of preparing capillaries with certain impedances was explored in a paper by Gauthier & Varoquaux [12]. They suggested filling the capillary with hard packed powder instead of a wire. The advantage would be that prediction of the capillary impedance factor is possible to within a factor of two. As noted by Gauthier et al. [13] it is difficult to predict the impedance of a capillary with a wire inside, necessitating a trial and error design method.

3.2 Heat conduction

3.2.1 Bulk heat conduction

Heat conduction is what thermal energy transport by means of a non-turbulent medium is commonly called. In a solid, thermal energy is transported by means of free electron movement and lattice vibrations (phonons). In a gas, it is conveyed almost exclusively by collisions between the gas particles. Primarily, heat conduction in solids will be studied here since convection is usually the dominant mode of heat transfer for fluids and gases.

In order to calculate heat conduction along pipes, rods and wires, the equation:

$$(3.1) \quad P = \frac{-1}{\int_{x_1}^{x_2} \frac{dx}{A(x)}} \left[\int_{T_1}^{T_2} k(T) dT \right]$$

which describes one-dimensional conduction of heat, was used [14]. $A(x)$ is the cross-section area, T_1 and T_2 the temperatures at the respective ends of the object and $k(T)$ the thermal conductivity function. P is the amount of heat transferred from the hot reservoir into the cold reservoir each second.

In N dimensions the heat conduction of a solid is governed by the partial differential equation below [15]:

$$(3.2) \quad \rho(\vec{r}, t) c(\vec{r}, t) \frac{\partial T}{\partial t} - \nabla \cdot (k(\vec{r}, t) \nabla T) = q_0(\vec{r}, t)$$

where ρ , c and k is the density, specific heat capacity and the heat conductivity, respectively. q_0 describes heat sources, which could be due to chemical reactions or absorption of radiation. This equation is already implemented in FEMLAB v3.0 for both transient and steady-state analysis; in the latter case the time derivate obviously disappears. It is interesting to note that for the steady-state analysis, the specific heat capacity of the involved materials will not affect the equations and thus the result.

However, for the specific case of thin shell elements in 3D, FEMLAB requires the heat equation to be implemented ‘by hand’ using its weak formulation.

The weak, or variational, formulation of the heat transfer equation is obtained through multiplication with a test function v and integrating the product on Ω , where Ω is the bounded domain. This is described in the MATLAB help files [16]. Using the same procedure, and noting that the heat conductivity is temperature dependent, the weak formulation of equation (3.2) in the steady state case becomes

$$(3.3) \quad \int_{\Omega} ((k(\vec{r}, T) \nabla T) \cdot \nabla v - q_0(\vec{r}) \cdot v) \cdot dx dy dz - \int_{\partial\Omega} (-aT + b) \cdot v \cdot ds = 0, \quad \forall v$$

where $(-aT + b)$ is the generalised Neumann boundary condition. Still assuming steady state, any solution T to equation (3.2) must then also be a solution to (3.3). A solution T to (3.3) is however more general and is only a solution to equation (3.2) under some additional conditions. It is therefore known as the weak solution to (3.2).

3.2.2 Contact resistance

In this thesis project, lack of time prevented the implementation of contact resistance into the FEMLAB simulation models. Therefore, no quantitative theory on the matter will be presented here, though a brief qualitative summary will be made.

The thermal conductance across a boundary between two dissimilar materials is usually rather low. This can be due in part to differing material structures, which inhibits the transport of heat due to acoustic or phonon mismatch. Using two blocks of, for example, Cu naturally eliminates this thermal resistance. A potentially far larger reason for a low thermal conductance however, is that material surfaces are seldom atomically flat. Hence, only a small part of the two material surfaces will actually be brought into direct contact with each other. Two ways to increase the contact area are to apply force – the more the better – and to coat the surfaces with very thin layers of a soft material that will fill up the cavities between the surfaces. Even if the soft material in question is not an outstanding thermal conductor, the large increase in contact area and the relatively thin layer of the material can greatly increase the thermal conductance across the boundary [17].

For cryogenic applications, Apiezon vacuum grease as well as Indium metal has proven suitable.

On an ending note, a contact resistance commonly referred to as Kapitza resistance appears between liquid ^4He and a solid as soon as the temperature drops below the λ -point. While this will not be of concern for the cryosystems in this thesis project, it is important to be aware of this phenomenon as it affects the performance of heat exchangers.

3.3 Radiative heat transfer

The aim of this section is to give a cursory description of the theory and calculations of radiative heat transfer in the ideal case of two concentric cylinders with metallic surfaces, separated by vacuum. It is hoped that this will demonstrate both the usefulness and limitations of a numerical treatment and an analytical solution.

In this section, the following concepts will be used:

- Grey surface: the radiative properties of a grey surface do not depend on the radiation wavelength.
- Diffuse emission/reflection: the emittance/reflectance of a diffuse surface does not vary with the direction of either the emitted or the reflected radiation, before or after the reflection. An example would be a sheet of paper.
- Specular reflection: the reflectance of a specular surface depends on the direction of both the incoming and the outgoing radiation. An example would be a mirror.
- Surface radiosity J : the total heat flux of diffuse radiation leaving a surface.
- Irradiance H : the total heat flux of radiation (diffuse or specular) entering a surface.
- Emissive power E_b : the emission heat flux of a surface, assuming it is black (meaning $\varepsilon = 1$).

Further, the reader is reminded of the blackbody equation [18]

(3.4)

$$E_b(T) = n^2 \sigma T^4$$

as well as the following surface and material properties [19]

$$\text{Reflectance, } \rho \equiv \frac{\text{reflected part of incoming radiation}}{\text{total incoming radiation}}$$

$$\text{Absorptance, } \alpha \equiv \frac{\text{absorbed part of incoming radiation}}{\text{total incoming radiation}}$$

$$\text{Transmittance, } \tau \equiv \frac{\text{transmitted part of incoming radiation}}{\text{total incoming radiation}}$$

$$\text{Emittance, } \varepsilon \equiv \frac{\text{energy emitted from a surface}}{\text{energy emitted by a black surface at the same temperature}}$$

It should be noted that all four are functions of both temperature and radiation wavelength for real surfaces and materials. Reflectance, absorptance, transmittance and emittance are often called reflectivity, absorptivity, transmittivity and emissivity instead, and they mean the same thing. It has however been recommended by NIST [20] that the latter alternatives only be used in the case of pure materials with a smooth surface, though in practise the terms are used interchangeably.

When analysing radiative heat transfer, it has to be kept in mind that in order to correctly analyse the net thermal radiation energy leaving one surface, all surfaces with which it can exchange radiation has to be considered. This includes surfaces with which radiation exchange can only take place through reflections in other surfaces. It may also include the surface exchanging radiation with itself, if it would be concave.

In the case of two concentric cylinders with metallic surfaces, it is acceptable to consider them grey. As described by Planck's law, the majority of the emitted radiation at temperatures below 300 K is at longer, i.e. infrared or thermal, wavelengths. In this spectral range, the radiative properties of most metals do not change noticeably with the wavelength.

They can also be considered diffusively emitting, something that is nearly always the case according to Modest [21]. They are however unlikely to be purely diffusively reflecting, necessitating a more complex treatment where they are considered as specular surfaces.

It is useful to realise that the added complexity is due to the necessity of including the direction of the radiation in the calculations. In the more simple cases of purely diffuse surfaces, the radiation field can, since no material or surface property depend on the direction of the radiation, be adequately described by the radiosity at the surfaces.

As an approximation, the reflectance of non-diffusive surfaces can be considered the sum of a diffuse and a specular part, i.e.:

$$(3.5) \quad \rho = \rho^d + \rho^s$$

With this assumption, a specular view factor can be introduced as:

$$(3.6) \quad F_{i-j}^s \equiv \frac{\text{diffuse energy leaving surface } i \text{ intercepted by surface } j, \text{ by direct travel or any number of specular reflections}}{\text{total diffuse energy leaving } i}$$

Other names besides view factor include configuration factor, shape factor and angle factor. The advantage of the above definition is that it removes the necessity of dealing with a directional radiation field from the rest of the calculations, allowing the use of surface

radiosity as mentioned above. All such considerations are included in the view factors. The disadvantage is that, except for special cases, the view factors are often difficult to calculate.

Assuming that an arbitrary geometry can be divided into a set of N isothermal sub-surfaces, the energy flux at a surface i in the geometry can then be written as:

$$(3.7) \quad q_i = q_{out} - q_{in} = (\varepsilon_i E_{bi} + \rho_i^d H_i + \rho_i^s H_i) - (H_i),$$

using the conservation of energy. The q :s are the averaged heat fluxes over the surface, E_{bi} emissive power as for a black-body, and H the irradiance. It should be noted here, that it has been assumed that the irradiance, the emissive power and hence the radiosity ($J_i = \varepsilon_i E_{bi} + \rho_i^d H_i$) is constant over the surface i . This is not necessarily true, although it is in the case of the surfaces of two concentric cylinders, due to axial symmetry. In the case of a complicated geometry, it can be treated as true provided an adequately extensive discretisation of the surfaces into polygons or other sub-surfaces. Alternatively, a spatial dependence can be introduced to the radiosity, irradiance and emission power and the view factors differentiated for a more rigorous treatment. This is outlined in [22].

Since the radiation leaving surface i diffusively, the radiosity, is $J_i = \varepsilon_i E_{bi} + \rho_i^d H_i$, the irradiance of a surface j , H_j , can be expressed as a sum using the view factors, surface areas and the radiosities. Using simple algebra along with the rule of reciprocity, which states that $A_i F_{i-j}^s = A_j F_{j-i}^s$ [23], the linear equation system below is obtained:

$$(3.8) \quad E_{bi} - \sum_{j=1}^N (1 - \rho_j^s) F_{i-j}^s E_{bj} = \frac{q_i}{\varepsilon_i} - \sum_{j=1}^N \frac{\rho_j^d}{\varepsilon_j} F_{i-j}^s q_j, \quad i = 1, 2, \dots, N.$$

If all surface temperatures, and hence E_b , are known for all surfaces the heat fluxes q for all surfaces can then be calculated.

As can be suspected, equation (3.8) has a simple matrix formulation and is easily solved by computer matrix inversion. Not surprisingly, the difficulty lies in calculating the view factors since they have to contain all information of the specular reflections. With the specular view factors defined as in (3.6), each view factor F_{i-j}^s must incorporate the contributions from every possible route diffusively emitted radiation from surface i can take to surface j no matter the amount of specular reflections on the way. This can be done by computer in the case of complicated geometries, though it can be time-consuming.

Luckily, in the case of two infinitely long, concentric cylinders, the specular view factors are easily obtained analytically as described by Modest [24]:

(3.9)

$$\left\{ \begin{array}{l} F_{1-1}^s = \frac{\rho_2^s}{1 - \rho_1^s \rho_2^s} \\ F_{1-2}^s = \frac{1}{1 - \rho_1^s \rho_2^s} \\ F_{2-1}^s = \frac{A_1/A_2}{1 - \rho_1^s \rho_2^s} \\ F_{2-2}^s = \frac{1 - A_1/A_2}{1 - \rho_2^s} + \frac{\rho_1^s A_1/A_2}{1 - \rho_1^s \rho_2^s} \end{array} \right.$$

Here surface 1 is the outer surface of the inner cylinder and surface 2 is the inner surface of the outer cylinder. Using equation (3.8) results in the heat fluxes:

(3.10)

$$q_1 = -q_2 = \frac{E_{b1} - E_{b2}}{\frac{1}{\varepsilon_1} + \frac{1}{\varepsilon_2} \frac{A_1}{A_2} - \frac{A_1/A_2 - \rho_2^s}{1 - \rho_2^s}}$$

Note that (3.10) will yield the same results regardless of whether the inner cylinder surface is specularly reflecting or not.

Further, it will be valid for any geometry where the view factors are identical with (3.9). This will be the case for geometries where $\rho_2^s = 0$ (i.e. surface 2 is a purely diffuse reflector), surface 2 encloses surface 1, and surface 1 can only radiate to surface 2. In this case there is no requirement that surface 1 and 2 have cylindrical shape and (3.10) is therefore no longer limited to concentric, infinitely long cylinders.

In closing this chapter, it is hoped that it has been demonstrated that analytical solutions are suitable only for very simple geometries due to the difficulties of calculating the specular view factors. If they can be found, they are quick and powerful to use. As soon as more complicated geometries are studied, numerical solutions are the norm.

3.3.1 Emissivity temperature variations

Unfortunately, most available values for material emissivity have been recorded for visible light at room temperature or at several hundred °C. The question of whether these values are of use in a low-temperature application where the interest lies in thermal wavelengths is therefore warranted.

As described by Modest [25], the Hagen-Rubens relation can be used to predict normal emittance trends for metals in the infrared. This means that assuming that $(T/\sigma_{dc}) \ll 1$, then $\varepsilon \propto \sqrt{T/\sigma_{dc}}$, where σ_{dc} is the electrical direct current conductivity. Since Hook and Hall states [26] that at extremely low temperatures the electrical resistivity will depend on material impurities, it will be independent of T. Thus, at liquid helium temperatures it will be reasonable to expect that $\varepsilon \propto \sqrt{T}$. At higher temperatures however, where the resistivity predominantly depends on phonon scattering, instead $\varepsilon \propto T$.

3.3.2 Multi-layered insulation

The aim here is only to give a very short, qualitative, description of one method of modelling the properties of multi-layered insulation, or MLI, as they apply to radiative heat transfer. For a description of MLI, see Appendix B.1.2.

A common method of modelling multilayered insulation blankets is to assign the surface they cover an ‘effective emittance’. This effective emittance generally depends upon the number of layers in the blanket, the radiative properties of the individual layers and the layer density. The latter has an impact since a higher layer density increases the risk of a conduction heat leak between two layers. Ideally, the layers should not be in contact with each other at all.

A few methods of calculating the effective emittance have been developed; they are however all empirical models, and there are still considerable difficulties involved in accurately predicting the performance of a given MLI blanket. This is mostly due to the difficulty of manufacturing and attaching an MLI blanket so that it corresponds to the blanket for which the effective emittance was predicted.

In this thesis project, no calculations of the effective emittance were performed. This was mostly due to the lack of a model that fit the MLI already used in the cryostat. Instead, different values were used in a number of simulations in an attempt to determine an effective emittance empirically.

3.4 Convection and Accommodation heat transfer

Convection

As convection did not play a role as a heat transfer process in the simulation models, it will only receive cursory attention in this section.

Analytically, the heat transfer by convection may be described by Newton’s law of cooling

$$(3.11) \\ P = hA(T_w - T_b)$$

where P is the thermal power transferred from a surface with area A and temperature T_w to a moving liquid or gas with bulk temperature T_b . h is an empirically determined heat transfer coefficient that depends on the fluid or gas properties, its velocity and the shape of the channel [27]. The difficulty of acquiring h limits the usefulness of equation (3.11), though some h functions for turbulent flows of cryogenic gases and liquids are given in the Handbook of Cryogenic Engineering [28].

Numerical simulation of convection heat transfer using physics application modes of FEMLAB v3.0 is possible, under some restrictions, and examples of convection models are given in the FEMLAB help files.

Accommodation

Accommodation is a heat transfer mechanism that appears at very low gas pressures, when the mean free path of a gas molecule is longer than the distance between two surfaces. Energy is then directly transmitted from one surface to another by means of gas molecules. Therefore, there are some similarities between accommodation and diffuse radiation, where heat is directly transferred from one surface to another by means of photons. However, the similarities should not be exaggerated.

Heat transfer by means of accommodation in the cryosystem as used by B. Nilsson while doing measurements on the ${}^4\text{He}(\gamma, n)$ reaction has been treated in the report on that experiment. The author agrees with the conclusion that with an isolation vacuum pressure

below the critical pressure of 0,44 mPa, radiative heat transfer will dominate over accommodation. For the full treatment, the author refers the reader to the Ph.D thesis by B. Nilsson [29].

In the case of the new cryosystem, all of the previous analysis by B. Nilsson is still applicable but the discussion needs to be extended to the volume between the 4,2 K Cu radiation shield and the LPC, which is not covered by the treatment. Unfortunately, both the more complicated geometry as well as the lack of information regarding accommodation parameters complicates the analysis. To achieve some sort of result, the rather coarse approximation of long, concentric cylinders is made even though the LPC cylinder is almost as wide as it is tall. Further, a worst-case assumption regarding to the accommodation parameters will set them to 1 for both the 4,2 K radiation shield and the LPC. The emissivity of both surfaces are set to 0,78, which corresponds to that of heavily oxidised Cu at 300 K. Unfortunately no reliable sources for oxidised Cu could be found for cryogenic temperatures. Assuming then a LPC temperature of 2,3 K, the equation utilised by B. Nilsson [30],

$$q_{a,1} = -q_{a,2} = \frac{A_1}{2} \cdot \frac{\alpha_1 \alpha_2}{\alpha_2 + \frac{A_1}{A_2} \cdot (1 - \alpha_2) \alpha_1} \cdot \frac{\gamma + 1}{\gamma - 1} \sqrt{\frac{R}{2\pi}} \cdot \frac{p}{\sqrt{T \cdot M}} \cdot (T_2 - T_1),$$

yields $q_{a,1} = 2,24 \cdot p \cdot A_1$ [W/m²]. By contrast, with the same assumptions equation (3.10) yields $q_{r,1} = 1,19 \cdot 10^{-5} \cdot A_1$ [W/m²]. The critical pressure would then be roughly 5,3 μPa. It is therefore likely that heat transfer by accommodation will be the same size as the radiative heat transfer between the 4,2 K radiation shield and the LPC, since the estimated isolation vacuum pressure after cryopumping was in the 1 μPa range.

3.5 Beam heat transfer

The photon beam that is going to be utilised for any measurements on a condensed ³He target is generated by the passage of an electron beam through a thin aluminium foil serving as a radiator. An absolute maximum of thermal energy conferred to the liquid ³He by the photon beam can then be estimated by starting from the electron beam power and then in turns calculate the power of the photon beam and then the total power deposited by the photon beam in the liquid ³He target. In reality, the amount of deposited thermal energy will be far less than the total power.

Assuming that the target temperature is 2,3 K, the target ³He density will be 75,2 [kg m⁻³] [31]. Radiator foil thickness t_{Al} usually varies between 50 and 300 μm, though typically a 50 μm foil is utilised in order to minimise effects from electrons interacting multiple times with the foil. With a target thickness t_{target} the energy removed from the photon beam, i.e. the energy deposited in the target, will be given by

$$\left. \begin{aligned} P_e &= N_e \cdot E_e = \frac{I_e}{e} \cdot E_e \\ P_\gamma &= \left(1 - e^{-t_{Al} \rho_{Al} / X_0(Al)}\right) \cdot P_e \approx 5,56 \cdot 10^{-4} \cdot P_e \\ P_{\max \text{ deposited}} &= \left(1 - e^{-7 t_{\text{target}} \rho_{\text{He}}^{(T=2,3)} / 9 X_0(^3\text{He})}\right) \cdot P_\gamma \approx 8,67 \cdot 10^{-4} \cdot P_\gamma \end{aligned} \right\} \Rightarrow P_{\max \text{ deposited}} \approx 4,82 \cdot 10^{-7} \cdot \frac{I_e}{e} \cdot E_e$$

where X_0 is the radiation lengths [32]. These can be calculated to within 5% accuracy by equation (3.12) below [33].

(3.12)

$$X_0 = \frac{716,4 \cdot A}{Z(Z+1)\ln(287/\sqrt{Z})} [\text{g cm}^{-2}]$$

A typical electron beam current I_e is 40 nA, with an average electron energy E_e of 250 MeV. With the coarse estimate above, a typical energy transferred to a 1 cm thick ^3He target by the photon beam would be 4,82 μW . Of this, only a small part will be thermal energy.

Assuming instead a ^4He target at 4,2 K that is 9 cm in diameter, which corresponds to the liquid ^4He target utilised in B. Nilsson's experiment, the above equations will yield a typical energy transfer of 54 μW .

4 FEMLAB model

Simulations of two cryosystems were made. The first was of the cryosystem set-up during a previously conducted experiment at MAX-lab by B. Nilsson [34]. The purpose of this simulation was twofold. First, it would provide experience working with FEMLAB. Second, it would allow some validation to be made of the model as data had been retained from the experiment on the cryosystem capacity. Unfortunately, the amount of data on the thermal aspect of the experiment was limited. Thus measurements from tests during the cryosystem reconstruction had to provide some data. Due to the oxidising copper radiation shields, performance had decreased since the experiment.

The simulation of the second cryosystem was intended to assist in the construction of the new cryosystem for ^3He condensation, through identifying sizes and details of different heat leaks. This was also realised to some extent, though the simulation of some heat leaks proved problematic.

4.1 Definitions

In this chapter, the term ‘geometry model’ will refer only to the modelled geometry without any equations and physics defined. Likewise, the term ‘physics model’ will primarily refer to the equations used to model the physics present in the cryostat and their implementation.

4.2 Short description of FEMLAB

As the goals of this thesis do not include promotion of specific software, only a short description of FEMLAB and its methods will be in order. For more information on this software package, please contact Comsol Inc.

FEMLAB is a software suite that allows equation based physics modelling. Its use has historically been tied to MATLAB, though the latest versions allow FEMLAB to run as a stand-alone product. FEMLAB can still run together with MATLAB and utilise MATLAB syntax and scripts.

As the name implies, FEMLAB is based on the finite element method. Several pre-defined application modes are available to the user, such as ‘Navier-Stokes’ for laminar flow simulations or ‘Conduction heat transfer’ for simulation of heat conduction. Using these modes, the equation systems are already defined and the user is left with defining the problem geometry using a CAD-interface, adding boundary conditions and the physical properties of materials. To cover those eventualities in which no pre-defined application mode fits, it is possible to enter the differential equations governing the system using the PDE (partial differential equation) modes.

FEMLAB also allows coupling of any of the application or PDE modes in order to simulate more complicated problems.

During this thesis project FEMLAB v2.3 – v3.0a was used mostly because of the features mentioned above. A few shortcomings with the vanilla software were however encountered. The most glaring was that FEMLAB v3.0 does not support simulation of radiative heat transfer. This is a considerable drawback for cryostat simulation, except for idealised geometries where such heat transfer can be described by analytical formulae. In such cases the analytical formulae can be used to describe the heat flux through a surface in FEMLAB.

During a FEMLAB workshop held by Comsol, the author was however informed that a future FEMLAB software module allowing calculations of radiation heat transfer is scheduled for release during September 2004. As it was thus not available for the duration of the project, all

heat transfer by radiation had to be implemented using approximations and analytical formulae.

Due to the extremely low temperatures and the large variation of material properties such as thermal conductivity, density and viscosity with temperature, functions had to be used when describing materials in the FEMLAB cryostat model. These were implemented in MATLAB and called from FEMLAB during simulation. For more information regarding the material property functions, see Appendix B.2.

4.3 Geometry model

4.3.1 Model optimisations

To start with, it should be noted that in order for FEMLAB to be able to calculate the problem in a reasonable amount of time and with finite computer memory resources simplifications had to be made when modelling the geometry.

First and foremost, model symmetries could be used to greatly decrease the amount of calculations necessary. While the finished cryostat and target will likely lack any vertical symmetry planes due to the placement of detectors and holes in the radiation shield, the preliminary model can ignore asymmetrically placed details through either adjustment of their position so that they become symmetric or ignore them altogether.

The ideal situation would have been rotational symmetry along the cryostat axis, which would have allowed the problem to be reduced to a two-dimensional problem in the (r,z) plane. Since this would have required removing all windows from all shields and the vacuum-chamber wall, the incoming photon beam would however have been greatly influenced and any meaningful measurements would have been rendered impossible. Small consolation then, that the cryogenic properties of the cryostat would have been vastly improved as well.

Further, in order to be able to simulate the radiation heat shields, these were modelled as 2D shell elements. An example is depicted in Figure 4.1, along with a cursory description of how it was created.

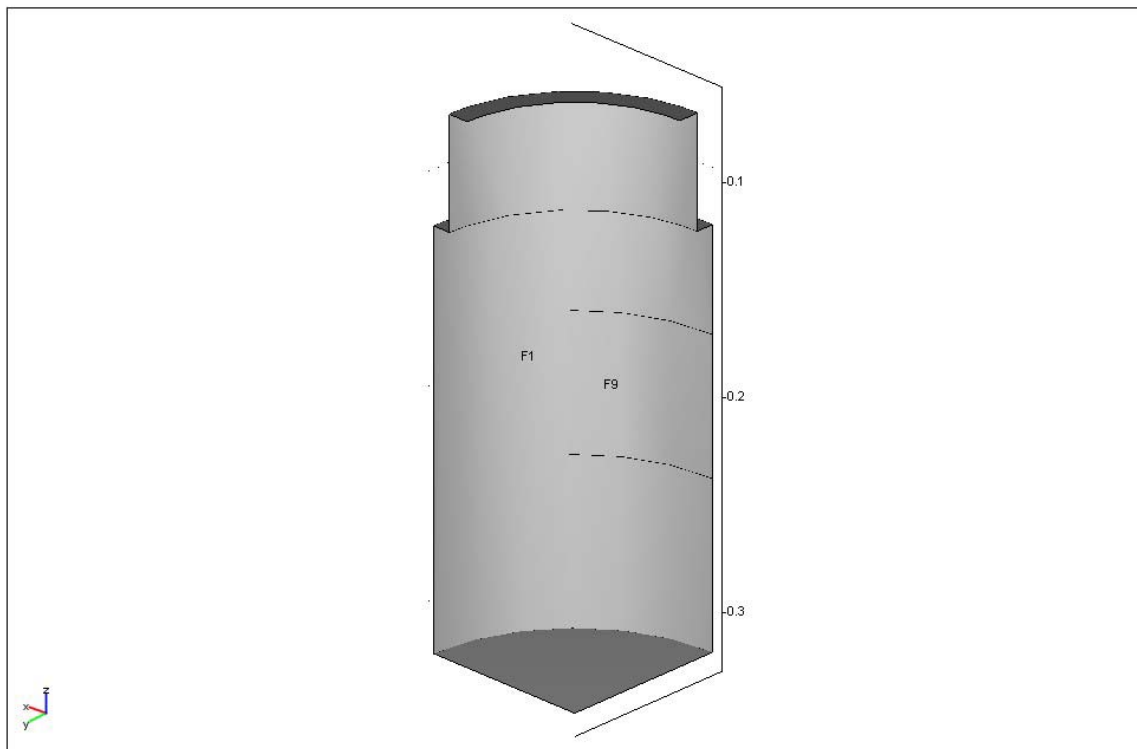


Figure 4.1: The picture displays the geometry model used for the liquid N₂ anchored radiation shield for the ³He condensation experiment. The radiation shield has been implemented using shell elements, created through first rotating an outline through 90° and then placing a rectangular block over the model so that an intersection between the shield and the block corresponding to boundary F9 was created. Marking all objects in FEMLAB and then choosing ‘coerce to face’ then broke down the model into its component faces, separating F9 from F1. Deleting the excess faces introduced by the rectangular block then yielded the above model.

4.3.2 Björn Nilsson experiment

The only part of the cryosystem that was deemed necessary to model with FEMLAB was the target area as shown in Figure 4.2. The reason for this decision was that the full cryosystem, a sketch of which is displayed in Figure 2.1, has a very simple geometry outside the target area. In addition, observations made during the experiment allowed the elimination of certain processes as contributors of heat to the liquid ⁴He bath. The heat transfer processes in these parts of the cryosystem could therefore be adequately modelled using analytical formulae or ignored. An example of the former would be radiative heat transfer from the reservoir radiation shield down into the liquid ⁴He bath; an example of the latter would be the complex interaction of heat transfers along the reservoir wall, between the wall and the rising ⁴He vapour and radiative heat transfer from the liquid N₂ jacket dewar to the reservoir.

As Figure 4.2 shows, the finished geometry model included the vacuum chamber, the liquid N₂-anchored radiation shield, the target and the lower part of the reservoir. The latter was assumed to be completely filled with liquid ⁴He. Any thin plates or foils were modelled as 2D shell elements. In the case of the target cell, the kapton foil and steel plate acting as the ⁴He container were modelled as surface boundaries on the ⁴He subdomain.

Due to the presence of two vertical symmetry planes, only one quarter of the true volume was modelled.

When modelling the copper radiation shield anchored to the liquid N₂ dewar, the radiation shield was considered to be made out of one piece. As Figure 2.3 shows, it consisted instead of one large frame of copper plate upon which five thinner copper plates were pressed using metal straps. This approximation was due to the following reasons:

- Major uncertainties were already present in the physics model, as the effective emittance of the MLI shielding and the copper plate proved elusive to determine. The small gain in accuracy from a more correct model would therefore have gone undetected.
- A completely correct shield model would have removed one symmetry plane, due to different plate thicknesses on opposite sides of the radiation shield. In coming projects where the ability to simulate radiative heat transfer numerically will be available, this may increase the time necessary for computation to unacceptable levels.
- Preparation of a geometry model of the radiation shield for the benefit of upcoming projects would in part have been wasted effort, as both the vacuum chamber and the radiation shields are due to be modified or replaced.

The MLI slits were implemented in the geometry model, due to the detrimental effect they may have on the heat transport in the aluminium foils. In the experiment they were drawn diagonally across the foil, and estimated to be 4 cm long and at most 1 mm wide. In the model they are implemented as being horizontal parallelograms with the length and width indicated above. This is a worst-case estimate since they will block the predominantly vertical conduction heat flow in the foil more effectively than had they been diagonal.

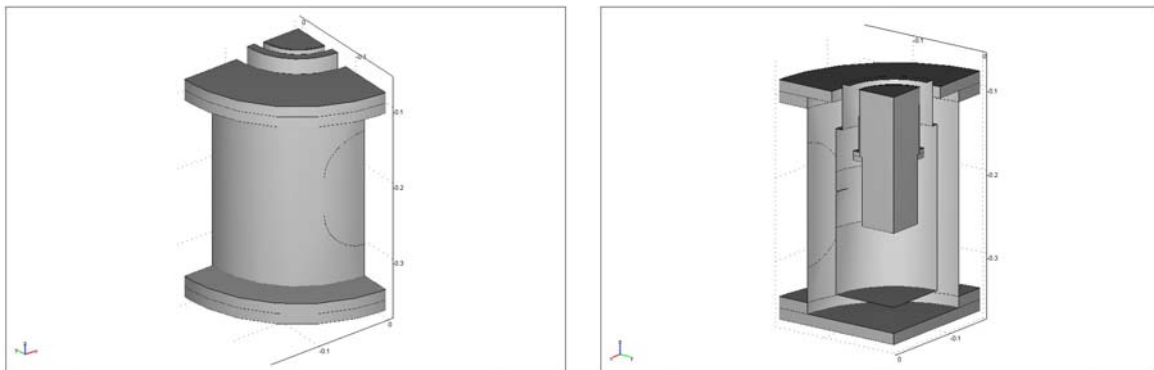


Figure 4.2: The geometry model utilised for simulations of B. Nilsson’s experiment, shown from two different angles. The solid block inside the reservoir and Kapton target represents the liquid ⁴He.

4.3.3 ³He condensation experiment

Several geometry model files were constructed for the simulation of the ³He condensation experiment. The file ‘3He experiment 20040429.fl’ includes the vacuum chamber and everything inside it, as shown in Figure 4.3. This is intended for future use with the coming radiation heat transfer module, although it is possible that considerable changes will need to be made to the cryosystem and hence parts of the geometry before that

The model file utilised for the ³He condensation simulation described in this thesis includes several geometries. They model the entire vacuum chamber, the bottom part of the reservoir, the LPC and the radiation shields.

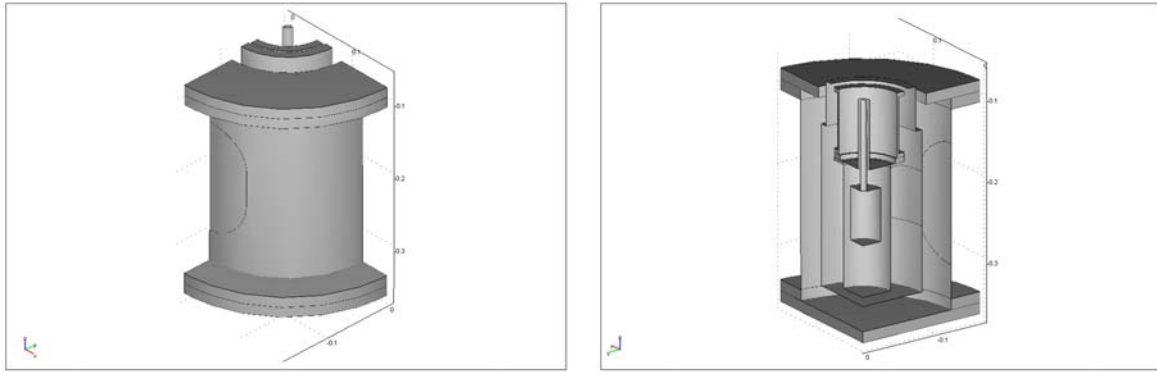


Figure 4.3: This image shows the geometry models made to simulate the set-up used for the ^3He condensation experiment, placed together. The simulations later used separate geometries for the LPC, the reservoir and reservoir anchored radiation shield, and the liquid N_2 anchored radiation shield. This was in order to save time, since a separate geometry could also be simulated separately from the others if the physics model did not connect them.

4.4 Physics model

In both simulations, only two of FEMLAB's application modes were utilised. These were 'Weak form, boundary, stationary state' and 'Heat Transfer by Conduction'. The former was only utilised for details represented by 2D shell elements in the geometry model, while the latter was utilised for the remaining details.

In the case of 'Weak form, boundary, stationary state', the weak form of the heat conduction equation (3.3) had to be entered using FEMLAB notation. To be more specific, the expression inside the first integral of (3.3), $((k(\bar{r}, T)\nabla T) \cdot \nabla v - q_0(\bar{r}) \cdot v)$ was entered as the weak term under 'boundary properties', while any boundary conditions were entered as constraints under 'boundary or edge properties'.

In order to obtain heat leaks into any body of liquid ^4He , the subdomain representing such a body had its surface temperature restrained to 4,215 K and its thermal conductivity greatly increased. This ensured that any heat flux into the subdomain exited at the surface and could be obtained by boundary integration, as well as keeping the subdomain at liquid ^4He temperature. While it is suspected that this is far from the most elegant method of obtaining heat leaks, it nevertheless sufficed as long as no outrageously large values for the thermal conductivity were chosen as this tended to influence the simulation results.

Regarding simulation of radiative heat transfer, two differing approaches were initially considered. The first was to simulate the heat radiation numerically in FEMLAB. The advantage would be a high accuracy in the results; this would be particularly desirable since earlier experiments had indicated radiation to be the largest and most important heat leak. The major disadvantage was that FEMLAB did not at the time of writing support detailed simulations of radiative heat transfer. Therefore either the author would have had to implement it himself via MATLAB or some other software or switch to other software that did support it. The second method would be to use emissivity calculations to make rough estimates with regard to the radiation transmitted by the different radiation shields in the cryostat. An advantage would be that it is a quick and not very complex way of solving the problem. Unfortunately, the disadvantage would be a lack of precision. Due to lack of the time required for the first option, either for an implementation or for learning a new set of software, the second approach was elected.

In the case of the cryosystems studied in this thesis project, convection heat transfer may be found in the reservoir and, for the ^3He condensation experiment, the pumping tube. Here the cold ^4He gas caused by evaporation of the liquid in the reservoir and the LPC rises and absorbs heat from the reservoir and pumping tube walls as it does so. The amount of heat transferred to the gas is of interest since it will not enter the LPC or the ^4He bath in the reservoir, allowing quantification of the amount of heat that does so via conduction along the walls. The gas will also cool the bottommost radiation shield in the reservoir, thereby limiting the amount of thermal radiation it emits towards the liquid ^4He bath. Equation (3.11) is however not very useful in any of these cases, as several heat transfer processes are at work simultaneously and neither T_w nor T_b is known. While FEMLAB simulation should be possible, it was judged too time-consuming to model during the course of this thesis project, for the following reasons:

1. Knowledge about ^4He gas properties as a function of both pressure and temperature is required, something that was difficult to obtain.
2. The PDE application mode would have to be used, since the gas flows are expected to be highly non-isothermal and turbulent. For either of these qualities there is a ready-to-use FEMLAB application mode, but not both. Hence implementation of the differential equations would be required.

In addition, results from the experiment performed by B. Nilsson showed that the amount of heat that reached the reservoir was negligible (see section 4.4.1, Radiative heat transfer: Liquid N₂ jacket dewar – reservoir wall). Thus the answer was already known, given a certain evaporation rate, reducing the importance of obtaining simulated values.

4.4.1 Björn Nilsson experiment

In this section the different heat transfer processes in the cryostat will be mentioned, along with their implementation and any assumptions and approximations made for that implementation.

It must be noted that a few heat leaks were not included in the FEMLAB simulation! These include the radiative heat transfer from the reservoir radiation shield to the ^4He bath, and the MLI slits. These were calculated separately using MATLAB m-files and then simply added to the simulation result.

Radiative heat transfer: Reservoir heat shield – liquid ^4He bath

When estimating the amount of heat radiated into the helium bath from the radiation shield at the top of the reservoir, some assumptions were made.

The first is that the reservoir walls are perfect reflectors as far as the radiation from the heat shield is concerned. This is not true – at room temperature even highly polished, stainless steel has only about 89% reflectance [35]. However, assuming this will allow all emitted radiation to reach the liquid helium since the reservoir walls will act as a beam-guide. This ensures that the calculations yield an upper limit of the heat transfer.

In reality, a considerable amount of radiation will be absorbed in the reservoir walls where a fraction will be conducted down into the helium reservoir and the rest transferred to the cold helium vapour rising in the reservoir.

The second is that the three holes in the radiation shield, that leads straight upwards to room temperature, can be ignored. This is assumed since they will be blocked by the pumping tube, a liquid He level meter and the liquid ^4He dewar transfer pipe. These will, as the radiation shield, be cooled by the rising helium vapour in the reservoir.

The third is that the radiation emitted by both the transfer pipe and the level meter can be ignored, even though they are made of steel with rough surfaces. This is motivated by both of

them being long, thin and parallel with the reservoir axis. Thus, due to their small surface area they will emit only a minor amount of radiation. Most of what they do emit will have to be repeatedly reflected against the reservoir walls in order to reach the helium bath, decreasing the intensity even more.

Under the above assumptions, the radiative heat emitted by the heat shield can be estimated by

$$P \approx \pi R^2 \cdot (\varepsilon_{Cu}(T = 82\text{K}) \cdot T^4 - 4,215^4)$$

where T is the temperature of the radiation heat shield. This temperature is roughly 82 K and was acquired through direct measurements on the preliminary set-up described in section 5.2.1.

Radiative heat transfer: Liquid N₂ jacket dewar – reservoir wall

In the case of the cylindrical liquid N₂ dewar that surrounds the ⁴He reservoir, they can be considered long, concentric cylinders. Thus the heat transfer would be given by (3.10). It is however problematic deciding where this heat goes. The amount that goes into the reservoir wall at or below the liquid helium surface is conducted to the ⁴He bath. The rest may either be conducted along the wall into the bath or absorbed by rising vapour. However, observations from B. Nilsson's experiment [36] indicate that little to none of the heat absorbed by the wall above the liquid surface actually reaches the liquid. It also indicates that the amount of heat is negligible in comparison to the amount that reaches the ⁴He through the Kapton foil target cell. This could be seen from the very linear decrease of the liquid ⁴He level with time; had conduction along the wall played a large part, the level decrease should have slowed due to the increasing distance to the hot areas. Likewise, the amount of thermal radiation from the liquid N₂ jacket dewar that enters the liquid ⁴He bath should have decreased the lower the ⁴He level in the reservoir thus leading to a slower level decrease the less helium there was. Since the decrease is linear with respect to time, as stated above, these two heat leaks must have been negligible in comparison to the amount of helium that boiled off in the Kapton foil target.

Hence this heat transfer process can be ignored in the present FEMLAB cryostat model, though it should be included in any simulation of the heat transfer and gas flow processes in the reservoir or for cryostats with much smaller heat loads on the target.

Possible errors will arise due to edge effects and the super insulation that the ⁴He reservoir is dressed with. The MLI blanket may be “crinkly” and thus the reservoir not exactly cylindrical, but most importantly the emissivity is expected to vary between different points on the blanket simply due to the unpredictable behaviour of MLI except under very controlled circumstances.

The wall of the liquid N₂ dewar is polished steel and is therefore approximated to be completely specularly reflecting; thus $\rho^s_2 = 1 - \varepsilon_2$.

Radiative heat transfer: Vacuum chamber - Liquid N₂ anchored radiation shield

In the case of the copper radiation shield protecting the target, difficulties arise with an analytical treatment. These are:

- The temperature of the copper shield is not constant over the area. It depends instead on the amount of radiative power incident on the surface and the thermal conductance to the liquid N₂ dewar, which acts as a thermal sink.
- The geometry is more complex, as the copper shield and the enclosure (the vacuum chamber) can no longer be considered as two concentric, long cylinders.
- The super insulation and aluminium foil with which the radiation shield is dressed is a specular surface.

A numerical treatment would therefore be preferred. As FEMLAB v3.0 and v3.0a did not at the time of writing support this, an analytical expression for the radiative heat flux nevertheless had to be used. The following assumptions and approximations were made:

- The radiation shield can be considered to be completely enclosed by the vacuum chamber, in the sense that all photons emitted from any point on the radiation shield must hit the wall of the vacuum chamber. Had the shield and its layers of super insulation been perfectly cylindrical this would indeed have been the case.
- The walls of the vacuum chamber are diffusively reflecting, i.e. $\rho_s^s = 0$. This is difficult to motivate properly; the walls are made of metal and while they are rough and can easily be seen as diffusively reflecting for visible light they are not necessarily so for thermal radiation, due to the longer wavelength. The assumption is made nonetheless.
- The vacuum chamber enclosure is isothermal and has a temperature T_2 of 300 K. As it is in direct contact with machinery and air at room-temperature, this is likely only a minor approximation.
- The radiation shield is isothermal and at a temperature T_1 corresponding to 77 K. This is not true; experiments with the old nitrogen shield yielded a likely maximum temperature around 87 K. As an approximation however, it will only have a small effect if equation (3.10) is used as $87^4 \text{ K} \ll 300^4 \text{ K}$. A rough estimate yields that the heat flux will be off with a maximum of 0,3%. This is deemed acceptable.
- The beam and detector windows present in the radiation shield are assumed not to be local hot spots, thus allowing the radiation shield to be treated as isothermal. This is supported by simulations, where the foils are not noticeably hotter than the shield, if their area is small enough (see Figure 7.3). Neither do they particularly affect the temperature distribution in the radiation shield.

With these assumptions, equation (3.10) holds and can be utilised.

Radiative heat transfer:

Liquid N₂ anchored radiation shield – reservoir bottom and target cell

In this case, almost the same assumptions and approximations as in the above case of radiative heat transfer from the vacuum chamber wall to the liquid N₂ shield are made. This time however, the liquid N₂ shield corresponds to the vacuum chamber while the Kapton cell target and bottom of the reservoir correspond to the liquid N₂ shield. The assumptions again allow equation (3.10) to be used. The motivations for the assumptions differ slightly in three cases however:

- The liquid N₂ radiation shield can no longer be considered isothermal at $T_2 = 77 \text{ K}$, due to the high sensitivity to T_2 (a power of four) in equation (3.4). As a coarse approximation T_2 is therefore set to the measured maximum local temperature of 87 K over the entire surface. This ensures that the calculated value of the heat leak is ‘worst-case’.
- The assumption that the reservoir bottom and target cell is isothermal at 4,2 K will not noticeably affect the result if equation (3.10) is used and the local thermal deviations are not abnormally large. Even should the true temperature be 20 K over the entire LPC the relative error will be less than 0,3%, which is acceptable.
- The assumption of purely diffuse reflections is as before difficult to motivate. Now, at visible wavelengths specular reflections can be seen in the frame of the radiation shield if not the attached plates. Nevertheless, in order to be able to do a rough estimate using equation (3.10) the assumption will be made. One should be aware that the error introduced by this will yield a higher heat transfer than the real one.

One additional approximation was however made. The emittance of the target and MLI clothed reservoir bottom differ greatly, which would automatically exclude the use of equation (3.10). Therefore an effective emittance for both the target and the reservoir bottom is used, but only when calculating the heat flux *out from* the liquid N₂ anchored shield. Due to the low temperature of the target and reservoir, an error in the effective emittance will not have that large an effect. To use an effective emittance when calculating the heat flux into the target and reservoir bottom however, would mean large local errors and unless a very good guess regarding the effective emittance was made also a large error for the sum radiative heat flux. Therefore, the individual emittances should be used for the target and the bottom end of the reservoir.

Radiative heat transfer: Liquid N₂ cooled radiation shield slits

The thermal radiation slipping through the two slits present in the radiation shield was considered to be completely absorbed by the target with none or very little heat going to the radiation shield. Since the slits were of the order of a mm wide, much larger than the wavelength of the spectral peak of 300 K thermal radiation ($\lambda \approx 10 \mu\text{m}$), diffraction effects could be ignored. The multiple layers of foil and MLI were also considered to provide a depth to the slits, which served to block out large-angle rays.

As an estimate of the amount of radiation that entered through the slits, the standard blackbody emission formula was used, $P = A \cdot \sigma T^4$. The absorptivity of kapton foil was approximated to 1 to provide a worst case scenario. Kapton foil, being an electric insulator (in most variants) is in any case expected to have a very low reflectivity due to low electron mobility. While its transmittivity at thermal wavelengths are unknown, all heat radiation that penetrates the foil will go directly to the liquid ⁴He bath and be absorbed.

This heat leak was calculated separately using MATLAB m-file 'heatleak_SLITS.m' and was not included in the FEMLAB model.

Beam heat transfer: Photon beam – liquid ⁴He

As detailed in section 3.5, the amount of heat deposited by the photon beam in the liquid ⁴He is roughly 54 μW . Compared to the size of other heat leaks, this amount is tiny and was therefore ignored in the simulation.

Conduction heat transfer: Liquid N₂ anchored heat shield – Liquid N₂ jacket dewar

When modelling the heat conduction of the liquid N₂ heat shield, the dewar walls were considered to be isothermal at 77 K. Since the dewar walls were thin and the dewar was filled with liquid N₂, this is a safe assumption.

In the case of the metal radiation shield bolted to the dewar, equation (3.3) was implemented using the FEMLAB PDE mode 'Weak form, boundary, stationary state'. The different thicknesses of the copper plates in the shield were entered through multiplication with the thermal conductivity function utilised. In other words, all plates or boundaries in the model with different thicknesses had different versions of equation (3.3).

The standing approximation made in the physics model was that there was no thermal contact resistance between the layers of the shield: copper plate, aluminium foil and MLI. The effect of this is that the copper frame and the MLI-blanket, including the aluminium foil, can be modelled through setting the emittance of the copper frame to that of the MLI. In effect, the effective emittance of the MLI blanket is the effective emittance of the blanket and frame. Another effect is that the heat conduction along the foil and the MLI is neglected. This should however not introduce that large an error, since the conduction of three layers of 0,03 mm Al foil and five layers of MLI each with Al coatings only 300 – 500 Å thick is small compared to a Cu plate roughly 1 mm thick at any temperature. Therefore almost all the heat will be

transported along the Cu plate and the effective thermal conductivity will be only slightly larger than that of the Cu plate.

Conduction heat transfer: Reservoir wall

All heat that may be conducted downwards along the reservoir walls is assumed to be carried off by the rising ^4He vapour. The motivation is exactly the same as in ‘Radiative heat transfer: Liquid N_2 jacket dewar – Reservoir wall’, to which the reader is referred.

4.4.2 ^3He condensation experiment

In this section the implementation of heat transfer processes in the simulation of the ^3He condensation experiment will be described. A few heat transfer processes in the B. Nilsson experiment and the ^3He condensation experiment are almost identical to each other; in these cases the descriptions will only be of the extensions or slight modifications to the arguments and formulae utilised in the previous section.

It must be noted that a few heat leaks were not included in the FEMLAB simulation! These include the radiative heat transfer from the reservoir radiation shield to the ^4He bath. Such heat leaks were calculated separately using MATLAB m-files and then simply added to the simulation result. The capillary conduction heat leaks, the lead heat leaks and the flow heat leak are also calculated separately using MATLAB m-files.

An attempt to implement the heat leaks in the FEMLAB model as point sources was made. However, this removed a vertical symmetry plane. This made the simulation too costly memory-wise for the computer rig utilised. While tweaking of solver settings likely would have solved the problems, lack of time prevented this.

Radiative heat transfer: Vacuum chamber - Liquid N_2 cooled radiation shield

This heat transfer process is identical for both the ^3He condensation and B. Nilsson’s experiment.

Radiative heat transfer:

Liquid N_2 anchored radiation shield - liquid ^4He anchored radiation shield (4,2K)

In the ^3He condensation cryostat, an additional radiation shield made out of polished Cu is used to protect the LPC from the thermal radiation coming in from the liquid N_2 shield. In this case, almost the same assumptions and approximations as in the case of the liquid N_2 shield are made. This time the liquid N_2 shield corresponds to the vacuum chamber and the 4,2K ^4He shield to the liquid N_2 shield. The assumptions again allow equation (3.10) to be used. The motivations for the assumptions differ slightly in two cases however:

- Instead of assuming the liquid N_2 radiation shield to be isothermal at $T_2 = 87$ K, the new measured temperature of 84 K is used. As for the simulation of B. Nilsson’s experiment, this ensures that the calculated value of the heat leak is ‘worst-case’.
- The liquid ^4He radiation shield is assumed to be isothermal at 4,2 K, as was the reservoir bottom and target cell for the simulation of B. Nilsson’s experiment. As before, this will not noticeably affect the result even if the true temperature of the shield is 20 K over the entire surface.

Radiative heat transfer: Liquid ^4He radiation shield (4,2 K) – LPC

Inside the radiation shield fastened to the bottom of the reservoir, the geometry is difficult to idealise. The LPC is a cylinder about as wide as it is high, with capillaries wound around it and soldered to the surface to ensure a good thermal contact. In addition the pumping tube suspending the LPC hanging inside the radiation shield is of a fairly large diameter. While almost all of the radiation emitted from the LPC will have to go to the radiation shield or

reservoir bottom, the extremely long wavelength of thermal radiation at 2-4 K will greatly increase the probability of specular reflections at the radiation shield surface. Hence, equation (3.10) can likely not be made to apply with only minor approximations.

Therefore, in order to get a worst-case scenario, four assumptions are made:

- All thermal radiation emitted from the radiation shield is absorbed in the LPC, i.e. that $q_{1,in} = \varepsilon_2 E_{b2} A_2 / A_1$. This ensures a worst case.
- All reflections on the surface of the radiation shield are specular. Moreover, the emittance of the LPC is assumed to be 1. Since this means all radiation emitted from the LPC is either absorbed in the radiation shield or reflected back towards and absorbed in the LPC, $q_{1,out} = E_{b1} \varepsilon_2$.
- The radiation shield is assumed to be isothermal with $T_2 = 11,2$ K, which is the measured temperature of its bottom plate. According to simulations, this is the hottest point on the shield.
- Radiative exchange between LPC and the pumping tube as well as between the radiation shield and the pumping tube can be ignored due to the (comparably) small exposed area of the pumping tube.

Accommodation heat transfer: Liquid ⁴He radiation shield (4,2 K) – LPC

This mode of heat transfer was not implemented, for the following reasons:

- Since the size of the heat leak is likely to be of the same order as the radiative heat transfer between the radiation shield and the LPC (see section 3.4), it will be extremely small in comparison with the heat leaks due to conduction along the capillary, gasline and pumping tube and the heat exchange with the liquid ⁴He flow refilling the LPC. It can therefore be safely ignored.
- The method used to estimate the accommodation heat transfer in section 3.4 is very coarse. Further, data regarding surface properties for accommodation were lacking. The accuracy of any estimate would therefore be highly questionable.

Mass flow heat transfer: Liquid ⁴He flow

Although the refilling of the LPC is a necessity, no liquid ⁴He at the same temperature as that in the LPC is available. Using the ⁴He from the reservoir, the only available option, will fill the LPC with heat as well as ⁴He, evaporating some of the ⁴He already in the LPC.

Assuming that the drop in temperature along the capillary is far quicker than the pressure drop, the size of the heat leak is roughly $P_{flow} = \dot{M} \cdot \Delta T \cdot c_p (p = 10^5 \text{ Pa}) \approx 4,49 \cdot 10^5 \cdot \dot{M}$ [W], assuming an LPC temperature of 2,3 K. The assumption is motivated by the pressure drop being spread out along the capillary while the heat exchange between flow and LPC will be the largest at the beginning, due to the larger temperature difference. Further, a more exact calculation would have to take the varying properties of liquid ⁴He in consideration as a function of both temperature and pressure. Such functions were unfortunately not available.

This heat transfer was calculated separately using a MATLAB function ‘heatleak_MASSFLOW.m’ and added to the simulated heat leak into the LPC.

Conduction heat transfer: Reservoir wall, outer wall of the pumping tube

Both these heat leaks are treated the same as the conduction heat transfer process along the reservoir wall in the simulation of B. Nilsson’s experiment, i.e. ignored. The motivation is however one more of convenience, than solidly supported by measurements. Since no attempt was made to measure the liquid ⁴He decrease in the reservoir over time, due to a lack of the latter, the motivation is merely that the pumping tube cross-section area is a very minor addition to that of the reservoir wall. Hence, there is no large increase in the amount of heat

that is conducted downwards and comparable ^4He vapour flows should therefore still be able to carry off all the heat.

Conduction heat transfer: Liquid N_2 anchored radiation shield – liquid N_2 jacket dewar

This heat transfer process is treated exactly the same as for the simulation of B. Nilssons experiment, and the reader is therefore referred to that section.

Conduction heat transfer: Liquid ^4He anchored radiation shield – reservoir

Exactly the same arguments as for the liquid N_2 anchored radiation shield apply here. However, since the radiation shield is polished Cu fewer approximations need to be made regarding effective emittance. The exact emissivity of Cu at 4,2K is not known, so as an approximation the value for 76K is utilised.

Conduction heat transfer: Reservoir – capillary – LPC

The heat leak introduced by the refill capillary between the reservoir and the LPC turned out problematic to simulate. The reason for this is the presence of a liquid ^4He flow through the capillary. In order to simulate or calculate the heat transfer correctly, the heat transfer coefficients between the capillary walls and the liquid ^4He would have to be known. In addition, the flow would have to be known along the length of the capillary. As earlier explained in 3.1, the flow by itself is difficult to simulate.

Therefore, in order to get an upper estimate of the heat leak introduced by the capillary, the approximation was made that no heat is transferred between the capillary walls and the liquid ^4He flow. The effect of this is that the heat leak along the capillary may be calculated using equation (3.1), and that the heat leak due to conduction via the capillary can be treated entirely separate from the heat leak due to the liquid ^4He mass flow. The motivation for the approximation is that at the junction between the capillary's steel and copper part, the 'hot' liquid ^4He flowing through the capillary will set the temperature to a higher value than it would otherwise have. This will limit the amount of heat that is conducted down to the junction from the reservoir. The heat that is conducted along the copper tube into the LPC will then to a larger degree come from the liquid helium flow. Since the liquid ^4He flow will have to be pre-cooled before entering the LPC in any case, this constitutes no performance loss. The unknown is how much heat that enters the LPC originally coming from the reservoir, i.e. the amount of heat that is conducted along the capillary nevertheless.

The approximation will therefore result in the conduction of heat into the LPC from the reservoir being maximised, providing a worst case value. This heatleak is calculated separately from the FEMLAB simulation using a MATLAB m-file 'heatleak_CAPILLARY.m'.

Conduction heat transfer: Liquid N_2 jacket dewar – ^3He gas line – reservoir

Under steady state operation, heat transfer along the gas line is assumed to be entirely due to conduction along the steel walls of the line with a minor heat conduction contribution from the ^3He gas in the line. The thermal contact conductance between the ^3He gas line and the reservoir bottom flange is assumed far greater than the thermal conductance along the continuing length of gas line down to the LPC.

Convection is ignored since it should be damped by the narrow channel with $\text{Ø}0,8\text{mm}$.

Hence, the heat leak can be calculated analytically using equation (3.1).

This heatleak is calculated separately from the FEMLAB simulation using a MATLAB m-file 'heatleak_GASLINE.m'. Should it be implemented as a point source in the FEMLAB model, it should be noted that due to the source lying on a symmetry plane the size of the heat leak must be halved.

Conduction heat transfer: Reservoir – ³He gas line – LPC

Under the same assumptions as used for the ³He gas line between the liquid N₂ jacket dewar and the reservoir, the heat transfer along the gas line can be calculated using equation (3.1). Implementation of the heat leak into the FEMLAB simulation would either require coupling two of the separate geometry models together, or approximating the temperature at the reservoir end of the gas line as 4,2K. This should not cause that large an error, since the bottom flange of the reservoir is in direct contact with liquid ⁴He at atmospheric pressure.

In the present model however, the heat leak is calculated separately using a MATLAB m-file ‘heatleak_GASLINE_LPC.m’.

Conduction heat transfer: Inner pumping tube – LPC

Due to the complex physics in the pumping tube, where gas flows and their interaction with conduction and radiative heat transfer processes need to be modelled, no attempt at modelling this in FEMLAB has been done. The large variations in ⁴He properties with temperature and pressure are expected to further complicate such a simulation.

Instead, the results from the ³He condensation experiment is relied on to provide data whether the net result is a large heat leak into the LPC or if the rising vapour do manage to carry off all heat before it reaches the LPC.

It can be said however, that the radiative heat transfer between the outer and the inner pumping tube wall will be negligible in comparison to the amount of heat conducted downwards from the top of the cryostat.

Conduction heat transfer: Electrical leads

Since all electrical leads to diodes and resistors placed in the target area during the ³He condensation experiment are anchored thermally to the liquid N₂ jacket dewar and then wound downwards along the reservoir and brought into thermal contact with the reservoir bottom flange by use of ordinary tape, equation (3.1) can be used to predict the thermal heat leak from the top of the cryostat per wire. Since the leads are roughly 1,5 m long and there are 14 leads going down towards the target area in total, the heat leak will be of the order of 0,13 mW.

This heat leak is calculated separately by use of a MATLAB m-file ‘heatleak_LEADS_RES.m’. Implementation into the FEMLAB model as point heat loads at the correct positions would necessitate the removal of both vertical symmetry planes, which is not a viable solution.

Electrical heating: Diodes

Since a constant excitation current is utilised in the 4-wire resistance measurement of the diodes, the heat load in one diode is given by $P = UI$. Typically, the voltage across a diode was 1 V at liquid ⁴He temperatures, with a measurement current of 10 μA. The electrical heating in a diode would therefore be roughly 10 μW, which will be negligible in most cases. They were thus not included in the FEMLAB model.

Eventual implementation into the FEMLAB model as point heat loads at the correct positions would necessitate the removal of both vertical symmetry planes, which is not a viable solution. Since the diodes were placed close to the cylindrical axis of the radiation shields, they could however be approximated as being placed at the centre. This would not remove any symmetry planes, though the heat load would have to be divided by four.

4.5 Simulation

This thesis project was intended as only a step in the development of a liquid ^3He target, rather than a separate work. As such, the thesis report must include instructions for how to run the FEMLAB simulations. This section is, more than any other part of the thesis, intended as an instruction manual and assumes that the user is familiar with FEMLAB.

In this section, settings and options used to correctly simulate the cryosystems will be described. Initially general comments on simulation and FEMLAB versions will be made, after which subsections on mesh settings, solver settings and initial guesses will follow.

All simulations were carried out using FEMLAB v3.0 and v3.0a with MATLAB 6.5.1. Initial work on physics models were made in FEMLAB v2.3b, though these were later discarded. In the author's experience, FEMLAB versions 3.0 and 3.0a were considerably more stable and user-friendly to work with.

An additional experience made by the author was that the rather complicated geometries of the cryosystems, which required a large amount of mesh elements for accurate simulation, was close to what could be handled by FEMLAB v3.0 and v3.0a without tweaking the solver settings extensively. The most common difficulty encountered when running the simulations was a lack of memory. While the PC utilised for the simulations was more than adequately equipped in this regard with 2 GB of RAM, FEMLAB requires an uninterrupted memory block. Hence, as soon FEMLAB tried to allocate a memory block that doesn't fit sequentially in the physical memory it will abort simulation.

4.5.1 Mesh settings

In general, only global mesh settings were manipulated. The adaptive solver (see section 4.5.2), which in FEMLAB is capable of refining the mesh during simulation should the mesh be too coarse, was however utilised.

4.5.2 Solver options

In all cases, a non-linear stationary solver was utilised since the theoretical models of radiative heat transfer are obviously non-linear due to the strong T^4 dependence. In the cases where the solution did not converge, the 'highly non-linear' option for the solver was therefore activated as a first step.

The preferred non-linear, stationary solver was the iterative solver 'GMRES'. While in FEMLAB v3.0a default settings were utilised, v3.0 required the selection of a preconditioner. In these cases incomplete LU-factorisation was selected in the form of the 'UMFPACK' preconditioner, with a drop-tolerance of 10^{-6} .

According to FEMLAB help files, direct solvers are usually slower than iterative ones for problems in dimensions higher than two, something supported by the author's experience.

In nearly all simulations, the general solution was calculated. The weak solution had been preferable, since more accurate heat flow calculations can be obtained in FEMLAB than with the general solution. However, in some cases, predominantly with FEMLAB v2.3, calculating the weak solution proved too demanding in terms of time and memory. In addition, the adaptive solver described below could not be utilised when calculating the weak solution.

The FEMLAB adaptive solver was utilised whenever possible. This allowed FEMLAB to adjust and refine the geometry mesh while solving the problem, should the solver encounter an area or volume where the local errors were too large. In some simulations, where the base mesh had a large number of elements, a maximum amount of elements was set above which the adaptive solver would not further refine the mesh. This was in order to avoid excessive memory use.

It was found that for the simulation of the ^3He condensation experiment, the calculated heat flows were not accurate enough. This could be seen from integrating the normal heat flux for

all boundaries of a volume. At steady state, since no volume had an internal heat source, this should have returned a very small numerical value (ideally zero). However, at times the returned value was of the same order as the enumerated total heat flow in the model. Hence, the weak solution was calculated instead. In addition, the error tolerances of both the non-linear and the linear solver were decreased by a factor of 10^6 in order to guarantee a more accurate result. This was successful, but was only attempted with FEMLAB v3.0.

It was noted that, if the adaptive solver was used, the geometry on-screen while the simulation ran would at times need to be re-meshed after the simulation was done. If not, it was not possible to re-run the simulation. This FEMLAB bug was observed in both versions v3.0 and v3.0a.

As an ending note, it might be prudent to mention that none of the models made during the course of this thesis support the use of a time dependent solver. In order to extend the physic models for simulation of time dependent processes, the weak form of the full, time dependent heat conduction equation (3.2) has to be implemented for the 2D surfaces. Presently only the steady-state equation (3.3) is implemented. This would also require heat capacity and density functions for every material utilised.

4.5.3 Initial values

It was found that the use of ‘good’ initial values reduced the amount of time necessary for the solution to converge. Therefore, guesses regarding the temperature were made for each sub-domain and shell-element in the model. However, simple guesses such as a constant temperature of 4,2K for the reservoir bottom flange or a linear correspondence between temperature T and height z for the model of the liquid N_2 anchored radiation shield sufficed.

5 Experiments

During the course of the project, several minor tests were run in order to obtain data for the simulations, both for use as validation and as input. Further, initial test runs on the cryostat after fitting the LPC using a single-walled pumping tube were used to calibrate two carbon resistors for use as temperature sensors. Toward the end of the project, an experiment in which both validation data for the simulation models was gathered as well as ^3He condensation attempted.

5.1 Equipment

In this section the temperature and pressure sensors utilised during the experiments will be described. Some information will then be provided on the evacuation systems used to provide both isolation vacuum and the low-pressure environment for the evaporation cooling of the LPC.

5.1.1 Temperature sensors

The primary thermometer used in the experiments was a DT-470-11A silicon diode sensor and a Model 218 temperature monitor, both purchased from LakeShore Cryotronics Inc. The diode had a sensitive range of 1,4 – 325 K, with a specified accuracy of 0,25 K in the 2-100 K range.

Further, two carbon resistors were utilised as thermometers. At very low temperatures, their resistance increases exponentially with decreasing temperature. In theory, this would make them highly sensitive temperature sensors at liquid ^4He temperatures. In a series of equipment tests, they were calibrated against the silicon diode. This limited the accuracy of the obtained calibration charts to the accuracy of the diode at the same temperature, which was nonetheless judged acceptable. The produced calibration charts for one of the resistors using different measurement currents can be seen in Figure 5.1.

For the high temperature calibration charts, as well as calibration charts for the second resistor, please see Appendix C:.

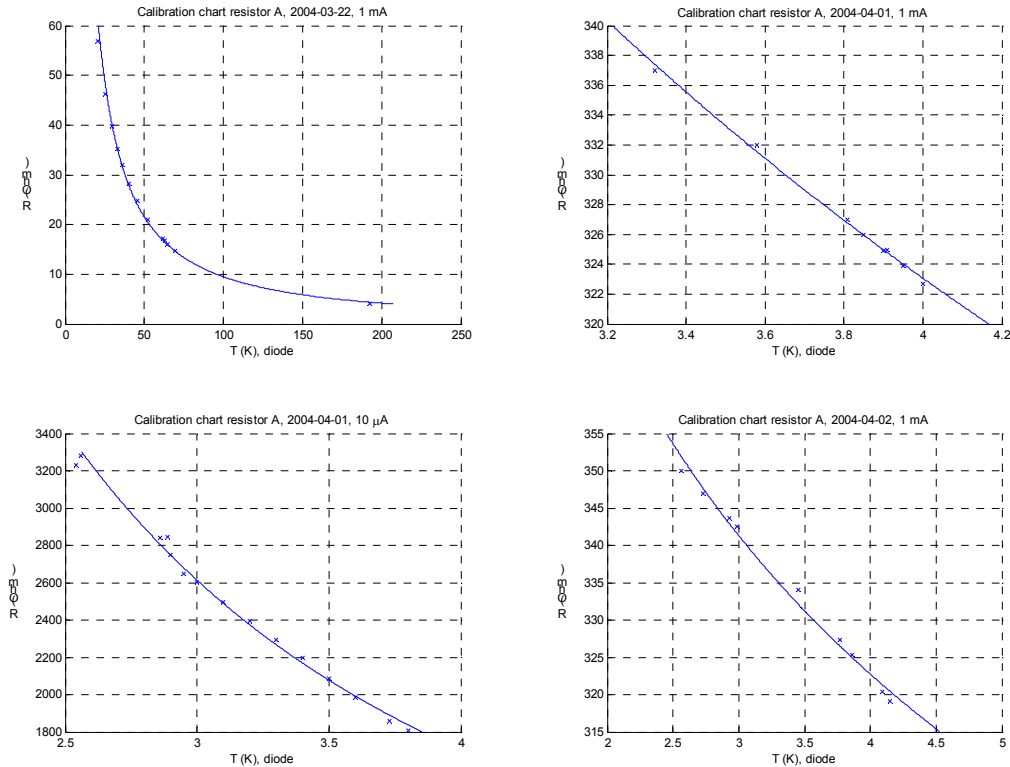


Figure 5.1: These figures show the calibration charts for a carbon resistor A used during the project. Solid lines represent a simple fit of an exponential function using the least-squares method. The upper left chart describes the $R(T)$ -relationship at higher temperatures. In the remaining charts, all describing the behaviour at low temperatures, the effects of electrical heating can be seen, as the data trend does not agree with the exponential function. Note in particular the huge difference in resistance between the use of 1 mA and 10 μ A excitation current for the measurements from 2004-04-01.

There were however several drawbacks to the resistors used as temperature sensors. Their construction included a cylindrical, gold-plated brass housing that made good and reproducible thermal contact with measurement surfaces difficult to achieve. Instead, the thermal contact was consistently rather poor and varied with each location at which the resistors were placed. During calibration, efforts were made to maximise the thermal contact using a copper bar to mount the resistors along with Apiezon vacuum grease on any contact surfaces. Such methods were however not always possible. This uncertainty in combination with a required minimum measurement current of 10 μ A resulted in a greater electrical heating of the resistors during measurements than during calibration. Thus, reported temperatures were consistently higher than that of the resistor environment during measurements. More worryingly, this error would be unpredictable and difficult to compensate for since the varying thermal contact would influence how much thermal power that could be dissipated and avoid a higher resistor temperature.

Hence, an attempt to calculate the accuracy of the resistors at lower temperatures was not even attempted. Instead, during experiments, the measurement current was varied to see if this influenced the reading. If not, then electrical heating was assumed not to noticeably affect the result and the calibration charts could be utilised.

All resistance measurements of the carbon resistors were made with a HP 34401A multimeter, using 4-wire connections. The electrical leads used for the low-temperature connections between sensors and measuring devices were QT-36 phosphor-bronze wires purchased from LakeShore Cryotronics. It should be noted that the dual requirements of low thermal

conductivity and high electrical conductivity are unfortunately exceedingly difficult to satisfy, since free electrons in a material contribute to both. Nevertheless QT-36 wire was deemed a suitable compromise as the lead diameter was small at 0,127 mm and the stated thermal conductivity of $48 \text{ [W m}^{-1} \text{ K}^{-1}]$ at 293 K about factor ten less than that of copper [37].

5.1.2 Pressure sensors

Three different pressures in the ^3He condensation cryosystem needed to be monitored. The isolation vacuum, the LPC pressure and the ^3He gas line pressure.

The isolation vacuum was monitored by an Edwards Penning 6 cold cathode ion gauge, capable of monitoring pressures from 1,3 Pa down to 13 μPa . Ability to measure such low pressures was necessary, since the isolation vacuum has to be as good as possible to reduce heat leaks by means of accommodation.

By contrast, the expected pressures in the LPC and the ^3He gas line were expected to be more moderate with around 6-7 kPa in the LPC and, initially, around 150 kPa in the gas line. Hence pressure sensors sensitive in completely different ranges had to be utilised.

The pressure in the LPC was monitored by a capacitance pressure gauge, calibrated against a fixed pressure cell. The gauge was a CFL-1000 sensor, read out using a Vacutec LPC-501 vacuumeter.

To measure the pressure in the ^3He gas line, something absolutely necessary in order to determine whether condensation takes place, a Barocel Electronic Manometer mod. 1173 was utilised. Should ^3He gas present in the gas line condense, the gas pressure would be required to drop.

It is important to note that all pressure sensors were mounted in ‘hot’ areas. The result of this is a higher reported pressure than in the cold parts of the same volume, due to cryopumping (see section 5.1.3).

5.1.3 Evacuation system

Two different evacuation systems were used in the cryosystem, one for the cryostat isolation vacuum and one for pumping on the LPC.

For the cryostat isolation vacuum a 2-stage mechanical SD-300 vacuum pump was used as a fore vacuum pump to evacuate the cryostat to a pressure of 300 – 400 Pa, after which a Turbo-V200 pump would take over and evacuate to the typical isolation vacuum pressures of 6,7 mPa. The Turbo-V200 pump had a stated pumping speed for He at 170 l/s. Both pumps were manufactured by Varian S.p.A.

The actual isolation vacuum pressure, measured in the hot parts of the cryostat after achieving steady state operation, was 0,47 mPa due to cryopumping. Filling the jacket dewar with liquid N_2 and the reservoir with liquid ^4He causes gas particles other than helium to condense and freeze, decreasing the pressure. This effect is most pronounced in the cold parts of the cryostat, where pressure sensors usually cannot be mounted. The actual pressure in the cold parts is estimated to be a factor 100 lower for a liquid ^4He cryostat of the designs utilised in this project.

In order to prevent the loss of the isolation vacuum should the turbo pump fail, an automatic valve between the turbo pump and the cryostat would isolate the cryostat from a rapidly rising pressure in the pump housing. This was judged an extremely important feature, since the loss of the isolation vacuum would result in huge heat transfers by convection between the reservoir, the liquid N_2 jacket dewar and the room-temperature cryostat housing. The result of such an occurrence would be an almost explosive boil-off of liquid ^4He and the cryostat would almost assuredly be ruined.

For pumping on the LPC, where pressures no lower than a few kPa were of interest, a helium leak detector ASM 110 Turbo from Alcatel was utilised. It was connected to the LPC evacuation pipe at the top of the cryostat by KF-couplings and the pumping speed regulated by a valve.

This unit was also used for all helium leak-seeking tests, since its built-in mass spectrometer was tuned to detect ions with an atomic weight per electron ionised of 2 to 4. In such cases it was instead connected to the exhaust of the Varian Turbo-V200 pump while helium gas was ‘sprinkled’ at cryostat joints and couplings to see if any gas leaked into the isolation vacuum volume.

5.1.4 Level probe

In order to monitor the liquid ^4He level in the reservoir and the LPC, a type 105 level probe from Cryogenic Ltd. was utilised along with its HLG200 instrument. The probe construction is basically a fine wire of NbTi alloy that goes superconducting below 10 K in the absence of magnetic fields [38]. The wire is shielded by a thin steel hose. Ideally, this would eliminate heat leaks due to electric heating during measurement since the resistance of the wire vanishes where it is subjected to low enough temperatures, such as when it is subjected to liquid helium or cold helium vapour.

Nonetheless, each time a measurement pulse was sent along the wire a surge in the reservoir helium vapour discharge was observed. This clearly indicated the need to limit the level sample rate order to avoid excessive helium boil-off. Since the two available settings of the sample rate were either 3 s or 3 min, the latter was utilised for any long-term measurements. For continuous operation of the cryostat for future experiments, it is recommended that the level probe be deactivated unless readings are to be taken.

5.2 Experimental set-up

In this section, the experimental set-up during calibration of carbon resistors and preliminary temperature measurements will be described, as it differs slightly in design from both the base and the redesigned cryosystem as described in section 2. Last details on the ^3He condensation experimental set-up will be provided, concentrating on placement and method of attachment of sensors and radiation shield MLI-blankets. As the main design will be identical to the redesigned cryosystem as described in section 2.3, it will not be further discussed under this heading.

5.2.1 Preliminary set-up

Since necessity demanded modifications to be made to the original cryosystem (described in section 2.1) continuously, some data and measurements that were acquired were taken from a cryosystem that was in a stage of development between the original cryosystem and the redesigned cryosystem used for the ^3He condensation experiment. This cryosystem was also utilised for the resistor calibrations.

The measurements taken during the cryosystem development were of the temperatures of the bottom of the liquid N_2 anchored radiation shield and the temperature of the radiation shield in the reservoir.

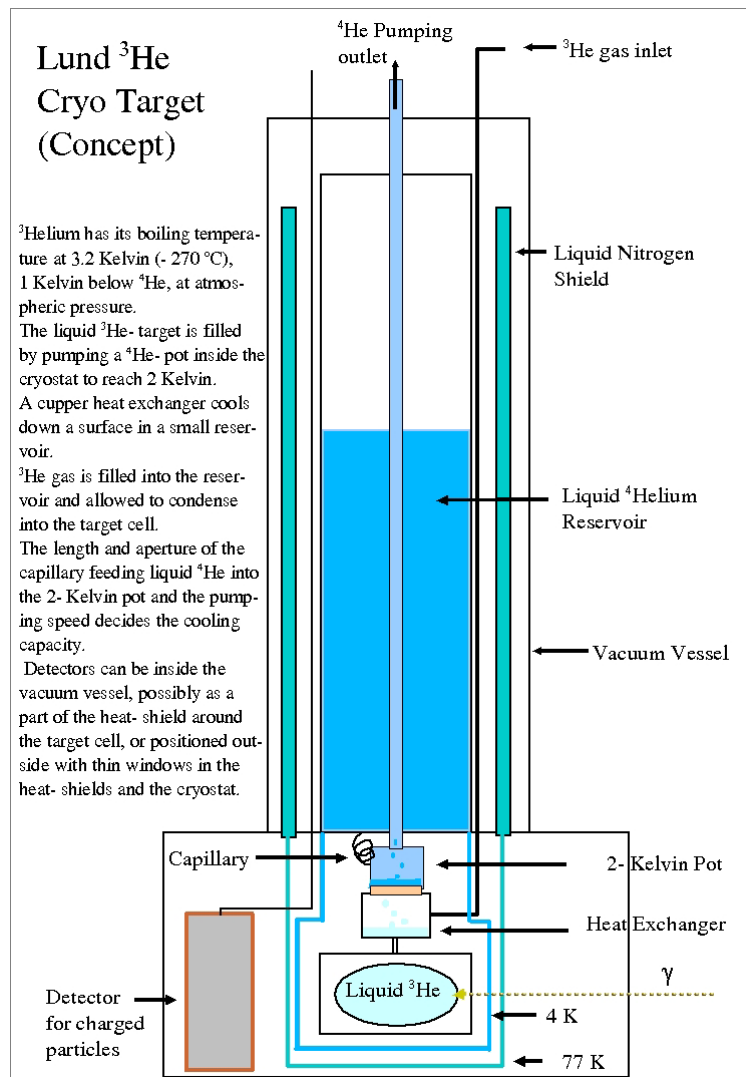


Figure 5.2: An early concept sketch of what became the preliminary set-up. Excepting the ^3He gas inlet, the heat exchanger, the detector and the actual target, the system was built and was utilised for calibration of two carbon resistors and measurements of radiation shield temperatures.

Figure 5.2 shows an early concept sketch of the preliminary set-up. The modifications made to the original cryosystem included the addition of an LPC with a single walled pumping tube in direct contact with the ^4He bath in the reservoir. A refill capillary between the reservoir and the LPC was included, though it was made entirely out of Cu with a steel wire inside to increase the flow impedance. These details are visible in Figure 5.3.

During the calibration of the carbon resistors, both resistors were mounted on the bottom of the LPC along with the DT-470 silicon diode using a copper bar. A thin layer of Apiezon vacuum grease was applied onto any contact surfaces in order to increase thermal contact conductance, as noted in the Handbook of Cryogenic Engineering [39].

After calibration measurements, preliminary temperature measurements were made of the radiation shield temperatures using the carbon resistors. Hence, these were placed on the bottom plate of the liquid N_2 anchored radiation shield and on the reservoir Cu radiation shield using Apiezon grease and ordinary tape.

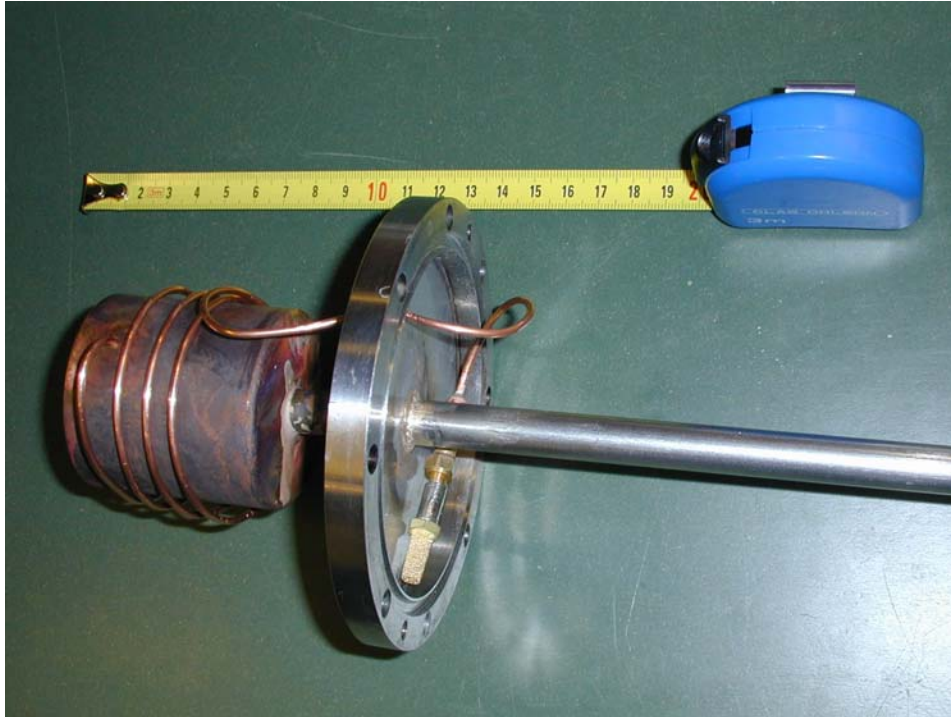


Figure 5.3: The image shows the LPC and pumping tube used in the preliminary set-up. The steel flange is bolted to the reservoir and acts as the reservoir bottom. In order to prevent cold leaks an indium seal was utilised. The refill capillary is made entirely out of Cu, save for the steel wire placed inside it to increase the capillary impedance. In the preliminary set-up, the capillary was not thermally anchored to the LPC, which makes the pre-cooling of the refill flow most inefficient. The pumping tube is a single walled steel pipe.

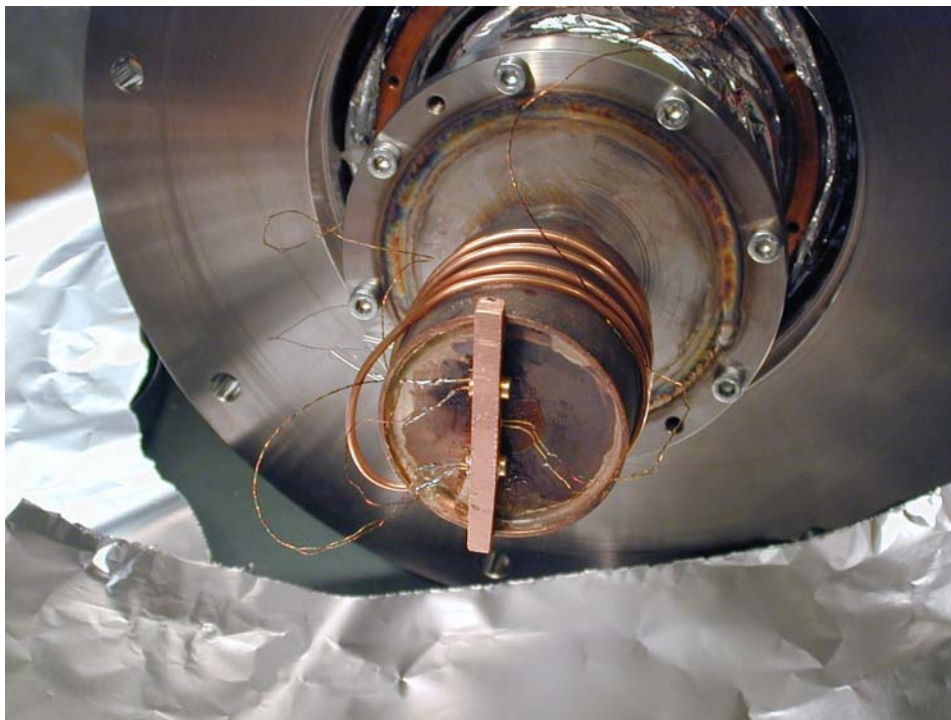


Figure 5.4: The image above shows the carbon resistor calibration setup. A Cu bar was utilised to attach both a silicon diode as well as both resistors to the bottom of the LPC. Apiezon vacuum grease was applied on any contact surfaces to improve thermal contact.

5.2.2 ^3He condensation set-up

The cryosystem set-up utilised during the ^3He condensation test was identical to the cryosystem as described in section 2.3. Therefore this section will only detail the location of and attachment method of the various sensors and MLI utilised for the ^3He condensation attempt.

For the ^3He condensation experiment, a small dummy volume was mounted on the heat exchanger as it exited the reservoir using two-component glue, as shown in Figure 5.5.

During the experiment, diode temperature sensors from LakeShore Cryotronics (see section 5.1.1) were mounted on the LPC and the bottom of the radiation shield bolted onto the reservoir, since they were the only two sensors sensitive at liquid helium temperatures available. The LPC mounted diode was attached by gently wedging it between the LPC and the ^3He capillary, as can be seen in the upper left picture of Figure 5.5. The radiation shield mounted diode was attached through the evacuation opening on the bottom of the ^4He anchored radiation shield, which can be seen in the upper right picture in Figure 5.5, using ordinary tape. Additional carbon resistor temperature sensors were mounted on the radiation shield at the top of the reservoir as well as on the bottom of the radiation shield bolted onto the liquid N_2 jacket dewar.

As noted in section 5.1.2, the Edwards Penning-6 gauge was mounted to monitor the cryostat isolation vacuum, while the pressure in the LPC was monitored by the capacitance pressure gauge and the ^3He gas line pressure by the Vacutec LPC-501 vacumeter.

Two level probes were utilised, one to measure the liquid helium level in the reservoir and one the liquid helium level in the LPC and pumping pipe. When mounting the probe in the pumping pipe, plastic distances were used to avoid direct contact between the level probe and the wall.

Additionally, a volume flow meter was utilised to measure the flow of helium gas from the reservoir and the LPC. While it could not perform both measurements at once, it was an easy operation to shift its position. For measurements of the reservoir gas flow, it was connected as indicated in Figure 2.1 while for measurements of the LPC gas flow it was connected to the exhaust of the pump used to evacuate the LPC. This ensured that the gas flow was of room temperature and atmospheric pressure.

Upon assembly of the cryosystem, Apiezon vacuum grease was applied to any contact surfaces where a good thermal contact was important. Such contact surfaces included all surfaces where temperature sensor were placed, as well as the surfaces upon which the radiation shields were bolted. It was noted when mounting the ^4He anchored radiation shield that a small gap was present between the inner part of the radiation shield flange and the reservoir bottom plate. After tightening the bolts, the gap was no longer visible from the outside though it may be possible that not the entire flange surface was brought into contact with the reservoir.

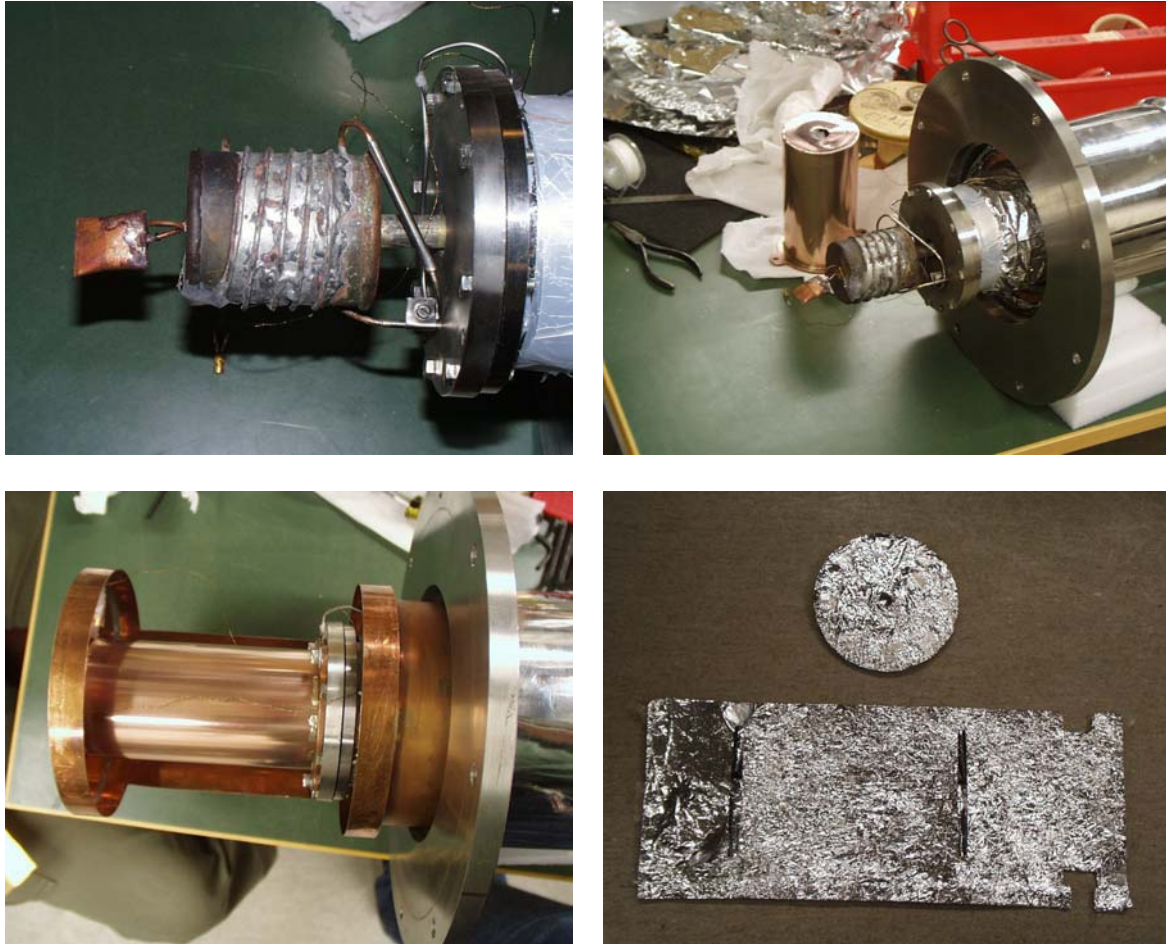


Figure 5.5: The upper pictures show the LPC, along with the refill capillary, ^3He gas-line and the small condensation dummy-volume. In the upper right picture the reservoir anchored radiation shield can be seen prior to attachment. The diode utilised for measuring the LPC temperature can just be seen at the LPC bottom. The lower right picture show the reservoir anchored radiation shield along with the Cu frame of the liquid N_2 anchored shield. The lower right show the MLI blankets with which the latter shield was clothed.

The MLI blanket covering the liquid N_2 anchored radiation shield consisted of two separate blankets, one circular intended for the shield bottom and one rectangular that was wrapped around the radiation shield. Both originated from B. Nilsson's experiment. After inspection of the mounted MLI, detrimental effects on the isolation performance was expected due to blanket joints and the ends of the metallic bands that strapped the Cu plates to the shield frame, which unfortunately penetrated the blanket.

Lastly, about three layers of aluminium foil were wound around the MLI blankets – taking great care that the foil would not be in contact with the hot 300 K vacuum chamber upon mounting the cryostat.

For future use of the cryosystem, a diode temperature sensor mounted onto whatever target is utilised is strongly recommended in order to correctly determine the liquid ^3He temperature and thus its density.

6 Experiment results

6.1 ^3He condensation

Cryostat start-up was achieved without major problems. After achieving an isolation vacuum of 0,47 mPa cooling commenced through filling the jacket dewar with liquid N_2 . As thermal equilibrium was achieved, the reservoir was filled with liquid ^4He . The total time for cool-down was of the order of three days, after which thermal equilibrium had been re-established in the cryostat

A few points about the cool-down were noteworthy. Before filling the reservoir with liquid ^4He , warm helium gas was allowed to flow through it and the LPC in order to flush out any other gases, primarily nitrogen and oxygen. These gases could otherwise solidify and accrete at the reservoir bottom. In particular, remaining traces in the capillary could solidify and block up the entire channel.

Cooling the cryostat from 300 K expended a great deal of cryogenic liquid, as the latent heat stored in the cryostat materials had to be transported away. Consequently, the initial fill of liquid N_2 or liquid ^4He resulted in a large boil-off and took about half an hour. In contrast, refilling the reservoir after cool-down had been achieved took ten minutes.

As in B. Nilsson's experiment, the gas flow from the reservoir was measured in order to obtain the size of the total heat leak into the reservoir. Originally, the intention was to fill the cryostat with liquid ^4He and let it stand overnight to ensure thermal equilibrium. However, due to time constraints and problems with a helium transfer line, it could only stand for four hours. The gas flow after those four hours was roughly $1,25 \text{ [dm}^3 \text{ min}^{-1}\text{]}$. This puts an upper limit on the heat leak into the reservoir at steady state, without pumping, at roughly 70 mW.

The carbon resistor mounted on the liquid N_2 anchored radiation shield reported a temperature of 84 K. The resistance of the resistor on the reservoir radiation shield varied depending on the boil-off rate in the reservoir; four hours after filling the cryostat with liquid ^4He the temperature reported was 34 K, though the value was not stable. At equilibrium, a higher temperature should be expected. That value should also be similar to the one obtained from measurements on the preliminary set-up, of 82 K.

Two measurement runs at temperatures below 4,215 K were made using the cryosystem set-up for ^3He condensation. An attempt to actually condensate ^3He unfortunately had to be aborted as a leak to the isolation vacuum appeared in the ^3He gas line. The sudden pressure increase in the isolation vacuum caused a convection heat leak to appear, with accompanying large boil-offs of liquid N_2 and ^4He as a result until the isolation vacuum reached low levels once again.

The intention during the measurement runs was to achieve steady-state operation while pumping on the LPC. The magnitude of the LPC gas flow would then directly correspond to the total heat leak into the LPC and the refill capillary flow.

The measured maximum temperature of the radiation shield bolted to the reservoir was $11,2 \pm 0,25 \text{ K}$. A quick estimate of the total amount of heat radiation a blackbody with the same surface and temperature as the radiation shield can emit yields only 52 μW . Further, accommodation heat transfer between shield and LPC will likely be of the same order as the radiative heat transfer, as the measured isolation vacuum pressure of 0,47 mPa leads to an estimated isolation vacuum pressure in the target area of 4,7 μPa due to cryopumping effects, which is roughly the same as the estimated critical pressure (see section 3.4) in the volume between the radiation shield and the LPC.

Since electrical heating of diodes are also in the μW range, as described in section 4.4.2, the only heat transfer processes into the LPC of notable size would be conduction heat transfer

along the ^3He gas line, the capillary and the pumping tube, as well as the heat carried by the ^4He refill flow. Then, knowing the refill capillary flow and the LPC temperature, determination of the mass flow heat transfer and the sum of the conduction heat transfers would be possible. In addition, the conduction heat leak from the ^3He gas line would be possible to calculate directly by using (3.1) since there are no gas flows through it. Conduction heat leaks along the pumping tube and the refill capillary would not be possible to calculate accurately however, due to the cooling effects of gas and liquid ^4He flows inside them.

It was however exceedingly difficult to achieve steady-state operation while maintaining large pressure differences between the LPC and the reservoir. After initiating pumping, maintaining an LPC pressure of 4,5 kPa was possible only for a few minutes during which time the liquid level in the pumping pipe steadily climbed. When the liquid column in the pipe reached the point where the walls of the double walled pumping pipe joined, the LPC gas flow climbed off the scale even if the flow meter bypass channel was fully opened. The evacuation system could then not maintain the pressure anymore, which started climbing.

This behaviour clearly indicates a gross over-dimensioning of the refill capillary. In the end, measurements could be taken on only two different steady-state conditions, which were achieved at LPC pressures of 93,6 kPa and 87,5 kPa. In both cases, the liquid ^4He column in the pumping tube came in the neighbourhood of the aforementioned wall joint. Measurements as well as calculated properties are presented in Table 6.1.

	Steady-state α	Steady-state β
<i>LPC level [m]</i>	0,85	0,86
<i>LPC pressure [kPa]</i>	93,6	87,5
<i>Gas flow, pump exhaust [$\text{m}^3 \text{s}^{-1}$]</i>	$50 \cdot 10^{-6}$	$110 \cdot 10^{-6}$
^4He temperature [K]	4,14	4,07
Maximum capillary heat leak [mW]	0,013	0,025
^3He gasline heat leak [mW]	0,0073	0,0140
Minimum pumping tube heat leak [mW]	168	362
^4He mass flow heat leak [mW]	3,17	13,3
Evaporation power removal [mW]	171	375
Capillary molar flow [mmol s^{-1}]	2,01	4,34

Table 6.1: The table above presents the measured quantities and calculated flows and heat leaks under the two different steady states α and β . Quantities in italics were measured directly, while the remainder was calculated. Of note is that the ^4He temperature has been calculated from the vapour pressure in the LPC rather than measured directly using a diode. This was done due to the large uncertainty in the diode measurements of 0,5K.

It can be seen that, due to the small temperature difference between the reservoir and the LPC, the conduction heat leaks into the LPC due to the capillary and the ^3He gas line are in the low μW region. They can therefore be ignored, as was the radiative and accommodation heat transfers. As the heat transported into the LPC via the liquid ^4He refill flow is only of the order of a few mW and the total heat leak is of the order of a few hundred mW, the vast majority of the heat leaking into the LPC must thus be due to conduction through or along the inner wall of the pumping tube.

In order to obtain some data regarding cryostat operation at temperatures in the 2 – 2,5 K range, observations had to be made on non-steady states. This was done through first emptying the LPC into the reservoir. Then the LPC was evacuated to as low a pressure as possible, after which the liquid ^4He level's increase with time was observed.

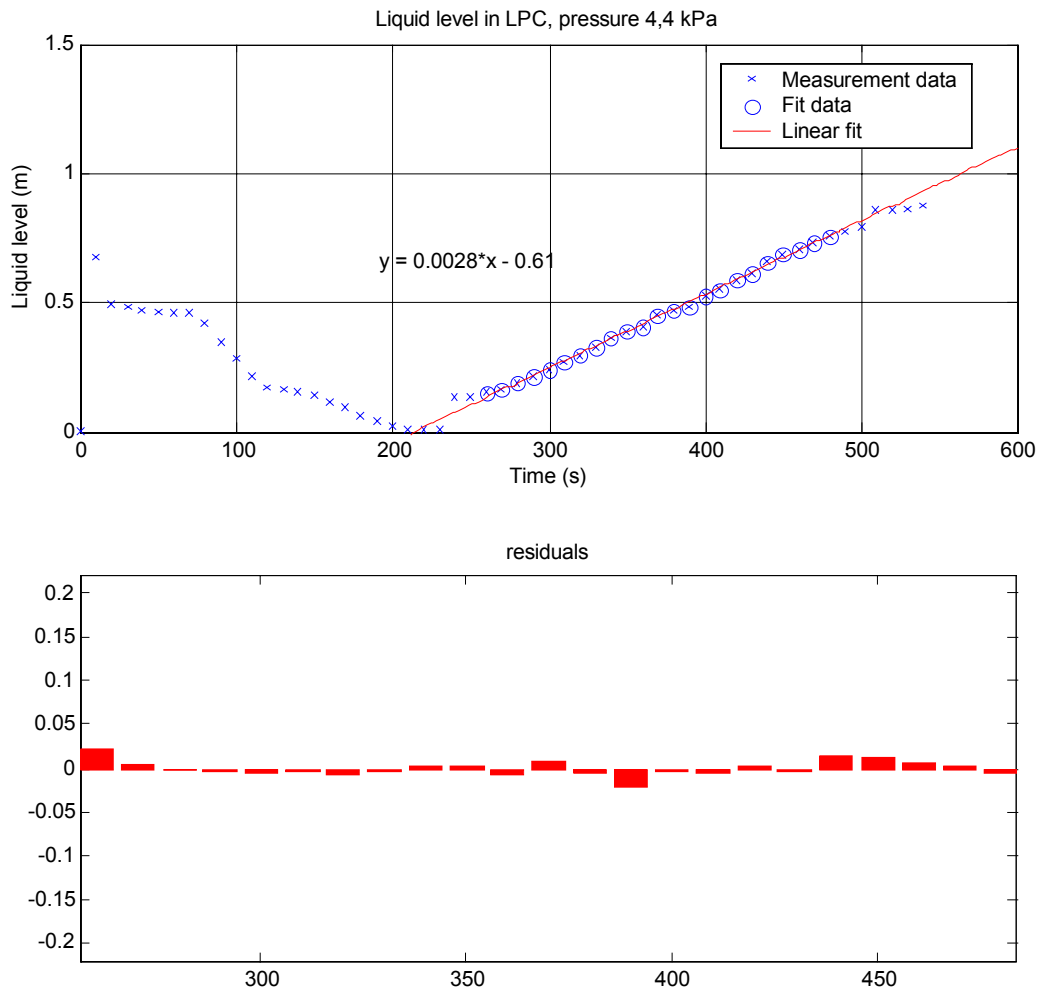


Figure 6.1: The top graph shows the liquid ^4He level inside the LPC and pumping tube as reported by the level probe. The time is in seconds after evacuation commenced, while the liquid level is the level as reported by the level probe, without compensation for the probe offset vs. the LPC bottom. The initial behaviour up to 250 s is believed to be due to various transient effects and does not represent the actual surface level. As an example, the increase of the liquid level under the first ten seconds, roughly 675 mm, is due to the sudden spike in the gas flow induced by the sudden pressure decrease. The bottom graph shows the residuals of the fit, which due to the random behaviour indicates that the increase of the liquid level is linear.

Allowing a small pressure difference between the reservoir and the LPC to build up through closing the pumping tube pushed liquid ^4He back into the reservoir and thus a low starting surface level in the LPC was achieved. Rapid evacuation of the LPC reduced the pressure to roughly 4,4 kPa within a few seconds, after which the pressure was stable. The liquid ^4He level then increased as indicated in Figure 6.1.

The linear increase of the liquid level, until the probe reports a level of roughly 860 mm, strongly indicates that heat conduction along the inner wall of the pumping tube does not play a part until the liquid column is in the neighbourhood of the wall joint. Otherwise, a gradual decrease of the level increase rate would have been noticeable in the plot. It should be noted however that the size of the gas flow through the pumping tube is very large; should a greater flow impedance than that of the current capillary be used the flow will be far smaller as will the cooling effect of the ^4He vapour on the pumping tube wall.

	Level increase measurement
<i>Pressure [kPa]</i>	4,4
⁴ He temperature [K]	2,13
Evaporation gas flow at 10 ⁵ Pa [l min ⁻¹]	10,6
Capillary molar flow [mmol s ⁻¹]	15,1
Capillary maximum heat leak [mW]	0,25
³ He gasline heat leak [mW]	0,14
⁴ He mass flow heat leak [mW]	650

Table 6.2: Table over the measured LPC pressure (in italics) and the calculated flows and heat leaks into the LPC.

The results gained from the level increase measurement can be used to calculate a few heat leaks, under the assumption that all heat leaks beside the ⁴He mass flow heat leak can be ignored. The measurement data and the calculated results are presented in Table 6.2, and are only applicable for the cryostat with the present capillary. Nonetheless, a few interesting observations can be made.

The first is that the cryostat is capable of operating at 2,13 K. Should a higher flow impedance be utilised, the mass flow heat leak and thus the evaporation gas flow will go down. This would likely allow a more efficient evacuation of the LPC and lower temperatures to be reached.

The second is that the calculated ⁴He temperature is just below the λ -point of 2,17 K and the LPC is thus filled with He II. Since the isolation vacuum pressure did not increase during the measurement run, the LPC and pumping tube does not have superleaks. Since there was some uncertainty regarding the accuracy of the capacitance pressure gauge, an additional attempt to reach lower pressures was made in order to be certain that the λ -point had been passed. Extra tubing, connections and the flow meter were removed to reduce the load on the pump. A reported pressure of 3,5 kPa, corresponding to a temperature of 2,04 K, was reached without any effect on the isolation vacuum. Since this reported pressure had been reached earlier with the preliminary set-up, and superleaks observed, the absence of superleaks is a safe conclusion.

While, as noted by Raccanelli et al. [40], this may introduce new heat leaks due to the generation of vibrations it is nonetheless a valuable characteristic. Replacing the current flow impedance could allow operation of the cryostat at temperatures approaching 1 K, which is the practical limit for cryostats based on pumping on ⁴He.

A third observation is that the calculated evaporation gas flow is just outside the scale of the flow meter. This is in agreement with experimental observations, since opening the flow meter bypass only slightly brought the gas flow within the scale again.

A fourth is that the temperature calculated from the ⁴He vapour pressure was substantially lower than that reported by the diode mounted upon the LPC. The stated uncertainty for the silicon diode in the 2 – 100 K range was 0,25 K, though during the attempt the diode reported temperatures around 2,9 K. This was around 0,8 K higher than that given by the vapour pressure. It was noted earlier, before pumping on the LPC commenced, that the temperature reported by the diode was 4,6 K instead of the true temperature of 4,215 K. This indicates that the diode is somewhat off. Whether this is due to the temperature being very close to the lower limit of the 2 - 100 K range, a bad thermal contact or simply a manufacturing fault is hard to say. Future use of the diode at liquid ⁴He temperatures should be possible, though calibration may be necessary.

A fifth is that the real conduction heat leak along the refill capillary is likely far smaller due to the large liquid flow through the capillary, as discussed earlier in section 4.4.2.

7 Simulation analysis

7.1 Björn Nilsson's experiment

Several simulations of the cryosystem utilised by B. Nilsson was performed, with differing assumptions regarding the emittances of the different surfaces in the cryostat. For a complete list of these simulations please consult Appendix A:

Validation of the simulations is unfortunately difficult due to the lack of measurements of the thermal performance of the different parts of the cryosystem. This is understandable, as the gathering of such information was not a priority at that time. The data available include the flow rate of the helium gas discharged from the cryostat [41], and the liquid helium level decrease over time in the reservoir as measured by a level-meter [42]. The former correspond to a calculated heat leak of roughly 115 mW, while the latter correspond to a total heat leak of roughly 150 mW. What the difference may be due to is unknown, but a possibility is an incorrect estimate of the temperature of the gas discharged from the cryostat. A lower temperature than the 0°C given by Nilsson [43] would account for the difference.

During the development of the ^3He experiment cryosystem, a temperature measurement of the bottom plate of the liquid N_2 radiation shield was taken using the preliminary set-up and can, to some extent, be used to validate simulations of B. Nilsson's experiment since the radiation shield had not been modified at that point. The copper frame will however have acquired a thicker oxide layer, with a possibly significant emittance increase. In addition, a temperature value for the reservoir radiation shield was acquired, though this value will rather be used as in-data for the heat leak calculations.

B. Nilsson notes that the vast majority of the heat that leaked in did so through the target cell in the bottom of the reservoir, something that could be observed from the very linear decrease of the liquid helium level [44]. This strongly indicates that the rising ^4He vapour, as expected, carries off the heat that would otherwise have been conducted into the helium bath along the reservoir walls (see 'Radiative heat transfer: Liquid N_2 jacket dewar – Reservoir', section 4.4.1). If this had not been the case, thermal conduction along the reservoir walls would have resulted in the heat leak decreasing along with the surface level of the liquid ^4He .

Discussions with K. Hansen [45], involved in the experiment, yielded the information that the ^4He target heat load had been strongly dependent upon the size of the slits in the radiation shield.

7.1.1 Simulation results

Due to the large amount of uncertainties regarding material properties, several simulations were run varying a few of those properties in order to examine their effect on the final result and whether the simulation produced reasonable results. Good agreement between simulation and the available data was expected to be due to chance, because of the many approximations made regarding radiative heat transfer in general and the large uncertainties regarding the cryostat materials and slit sizes in particular.

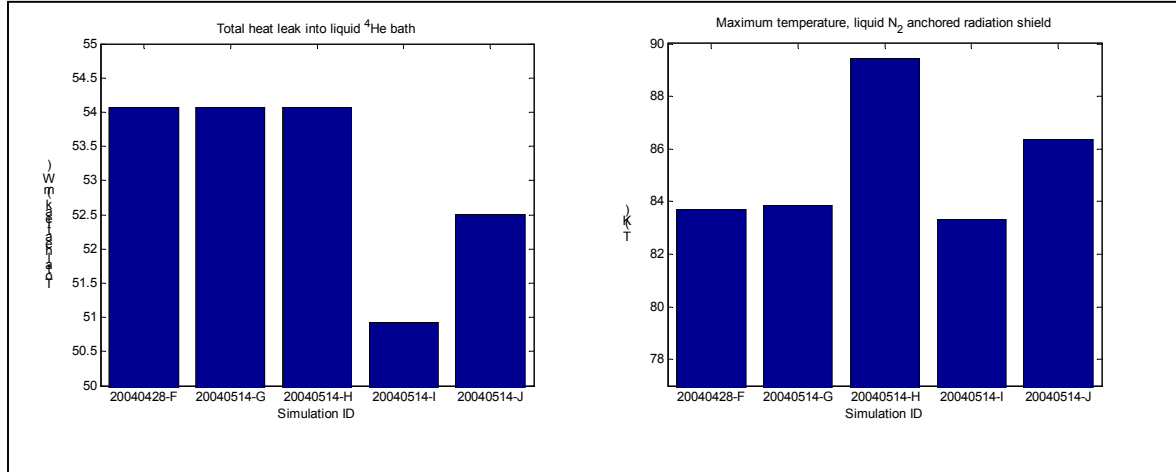


Figure 7.1: The simulated total heat leak into the liquid ^4He for B. Nilsson’s experiment, including the heat leak from the slits and the reservoir radiation shield, is shown in the left graph for five different simulations. The right show the maximum temperature of the liquid N_2 anchored radiation shield. Please note that the vertical scales have been truncated.

Simulation ID	$k_{\text{Cu}}(T)$	MLI ϵ_{eff}	Target ϵ_{eff}
20040428-F	OFHC Cu	0,060	0,5
20040514-G	OFHC Cu	0,060	0,9
20040514-H	Cu RRR=20	0,060	0,5
20040514-I	Cu RRR=20	0,030	0,5
20040514-J	Cu RRR=20	0,045	0,5

Table 7.1: A table listing the simulation properties for the simulations in Figure 7.1. The thermal conductivity column indicates what Cu material the liquid N_2 anchored radiation shield was assumed to be made of.

It was found that the thermal conductivity of the copper in the liquid N_2 anchored shield strongly influenced the shield temperature, which indeed was to be expected. This can be seen in Figure 7.1, where simulation H has assumed a thermal conductivity of the Cu in the shield half that of OFHC Cu. This value should be compared with that of simulation F, which uses the same assumptions save for Cu thermal conductivity, where OFHC Cu is assumed. According to the Handbook of Cryogenic Engineering [46], the thermal conductivity of Cu RRR=20 (a lower degree of purity than OFHC) is roughly half that of OFHC Cu.

It should be noted however that assuming half as large a thermal conductivity is equivalent to assuming half as thick a Cu plate.

The MLI effective emittance can be seen to influence both the radiation shield temperature and the total heat leak into the ^4He bath. The effect on the radiation shield temperature from halving the MLI ϵ_{eff} is expected, as the amount of thermal energy pumped into the shield radiatively from the vacuum chamber and has to be conducted to the liquid N_2 jacket dewar sharply decreases.

Likewise, the effect on the total heat leak is expected, since the MLI covering the bottom end of the reservoir reflects a large part of the incoming radiation. Halving the MLI ϵ_{eff} will then affect the amount of radiative heat that is absorbed. Since the Kapton target cell is not covered with MLI however, the effect on the total heat leak is only minor. Due to the already low value of ϵ_{eff} in 20040514-H, a majority of the heat leaking in radiatively to the ^4He bath does so through the Kapton foil. Decreasing the amount coming in through the MLI blanket covering the bottom end of the reservoir will not provide a major improvement.

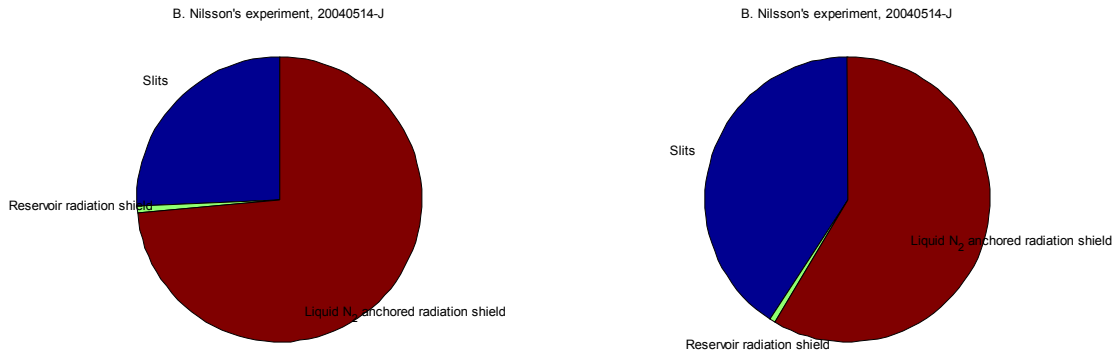


Figure 7.2: The pie charts above indicate the origin of the heat leaking into the liquid ^4He bath. In the chart on the left, slits have been assumed to be parallelograms 4 cm long and 1 mm wide while in the chart on the right they have been assumed to have twice the area.

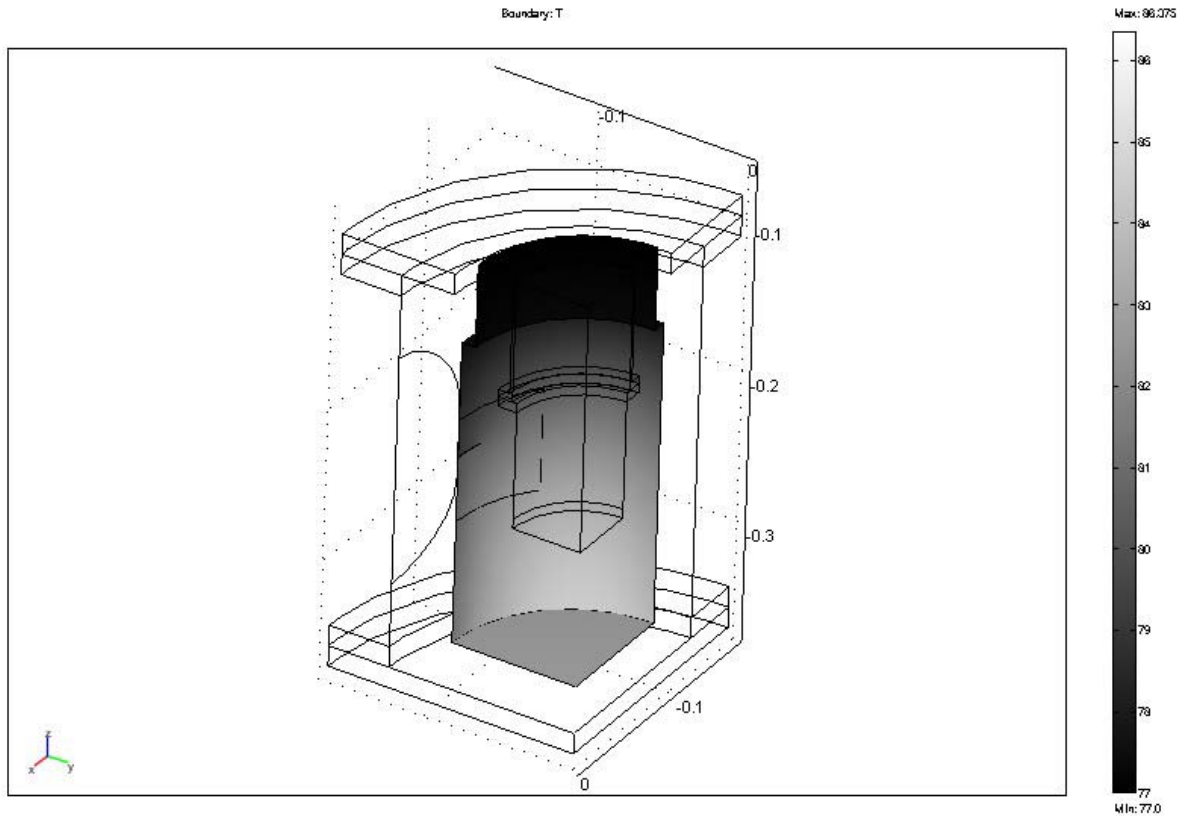


Figure 7.3: The simulated temperature distribution in the liquid N_2 anchored radiation shield, in simulation 20040514-J. The spatial scale in the image is in meters, while the temperature scale is in degrees K. Note that the temperature scale has been truncated. The outline shows the vacuum chamber, the Kapton foil target and the bottom end of the reservoir.

Figure 7.2 indicates that according to the simulation, a clear majority of the heat entering the liquid ^4He bath does so via radiation from the liquid N_2 anchored radiation shield. This is however greatly dependent on the size of the radiation shield slits, which has been assumed to be 4 cm long and at most 1 mm wide.

7.1.2 Simulation validity

A comparison between simulations 20040428-F and 20040514-G clearly indicates the minor effect the effective target emittance has on the result of the simulations. Thus the approximation made in the physics model (section 4.4.1) to replace the Kapton emittance and the MLI ϵ_{eff} with the target ϵ_{eff} will not, even if the estimated target ϵ_{eff} is wrong, noticeably affect the result.

Further, the assumption that the MLI blanket covering the radiation shield holes will not maintain a noticeably higher temperature is not in contradiction with the simulation result, as can be seen in Figure 7.3. It should however be noted that the simulation assumes no thermal resistance between the MLI blanket and the Cu radiation shield frame. Should this not be case in the real cryosystem, a ‘hot spot’ may very well appear despite what the simulation show. If so, thermal contact between the MLI blanket and the Cu frame along the hole edges will have to be enhanced in order for the simulated situation to be applicable.

The simulations showed an expected heat leak into the liquid helium in the cryostat target area is of the order of 50 – 55 mW, excluding heat leaks due to the reservoir radiation shield and the slits in the MLI covering the liquid N₂ anchored radiation shield. The estimated heat leak from the reservoir radiation shield was 0,56 mW while the estimated heat leak from the slits was roughly 18 mW and as shown in Figure 7.2 very dependent upon the estimated slit area being correct. This only accounts for about half the amount that corresponds to the observed boil-off during the experiment.

Several errors can be identified as having a large effect on the result:

- The actual slit sizes during B. Nilsson’s experiment were not available in the documentation to which the author had access. As has been seen, the sizes of the slits greatly influence the amount of heat that enters the target area and they can easily account for a large part, or even all, of the ‘missing’ energy. This is supported by the experimental observation that the ⁴He boil-off rate greatly depended upon the size of the slits. Since they from the target’s point of view acted as direct windows to the 300 K vacuum chamber, this was not surprising. Unfortunately, they were necessary for measurements of the target ⁴He density and were thus required.
- The, in the simulation, assumedly perfect thermal contact between the aluminium foil and the copper frame is of course incorrect. How large an effect it has on the final results are however uncertain. Should there be virtually no thermal contact the temperature of the aluminium foil where it is visible for the target will be far higher. This will be due to the lower thermal conductivity of aluminium versus copper as well as the foil being thinner. Thus, radiative heat absorbed in the foil will not be able to be carried off as effectively. However, since the foil is in direct contact with the copper frame in numerous places, radiative heat exchange between the foils and the frame will work to equalise their temperatures, and the temperature of the aluminium foil in the simulations were far lower than at the bottom of the copper frame, it is assumed that this will not markedly affect the result and the error should have been more than compensated by the ‘worst case’ assumption that the entire shield has a temperature of 87 K rather than just the bottom.
- The sheer number of approximations made when trying to calculate the radiative heat transfer likely has a considerable effect on the result. Unfortunately, where possible, worst-case approximations have been used. Hence, the simulated total heat leak ought to have been larger than the observed.
- The lack of data on material properties, such as emittances and thermal conductivities, can unfortunately have a large influence on the result as shown by Figure 7.1, since guesses are unavoidable. While it was always known which material had been used for the different details, the purity (in the case of Cu) or the exact alloy specifications (in

the case of stainless steel) was always in doubt due to the lack of documentation available on the cryostat.

The author's conclusion is that, due to the multitude of error sources, no conclusion regarding the applicability of the model on B. Nilsson's experiment can be made. It can however be noted that the size of the calculated total heat leak is off only by a factor 2, which due to the amount of error sources must be considered satisfactory. The model can certainly be improved; the first step should be to determine correct material properties or simply replace cryostat details with unknown properties, which may very well be easier. The second step should be to numerically model the radiative heat transfer, which will in one stroke remove a whole slew of assumptions and approximations. Should this be done in a future project, the author would certainly be interested in the discrepancy between the numerical simulation and the model developed during the course of this thesis project.

7.2 ^3He condensation experiment

Validation of the FEMLAB simulation of the ^3He condensation experiment is slightly easier, as more data on the cryostat thermal performance is available from the ^3He condensation experiment than what was gathered during B. Nilsson's experiment.

Specifically, thermal data on the different radiation shields in the cryostat is available as temperature sensors were placed on each shield. Further, a rough upper limit on the total heat leak into the reservoir at steady state is known from the boil-off of liquid ^4He . Had the gas flow been measured when thermal equilibrium had been established, instead of after just four hours, the boil-off would have corresponded exactly to the heat leak.

Heat flows into the LPC under two different steady states are also available from the experiment. Unfortunately, in both steady states the LPC and the pumping tube is completely filled with liquid ^4He . The supposition in the prepared geometry models was, perhaps unrealistically, that the flow impedance would have been balanced so that the liquid ^4He level would have been inside the LPC rather than at the top of the cryostat. Further, the only heat transfer process into the LPC that is simulated in FEMLAB is the radiative heat transfer from the radiation shield bolted onto the reservoir. Like the analytical argument made in section 6.1, all simulations show this heat transfer is extremely small. Since the measured heat leak into the LPC is due mainly to conduction and the ^4He mass flow, this part of the FEMLAB simulation cannot be validated from the acquired data.

The data acquired from measurements of the cryostat's low-temperature behaviour is less useful for simulation validation, since all the simulations assume that thermal equilibrium has been achieved.

7.2.1 Simulation results

Using the data acquired from the ^3He condensation experiment, several simulations were run. Since there were large similarities with the simulations of B. Nilsson's experiment, there was less emphasis on exploring the effects of different choices of material parameters.

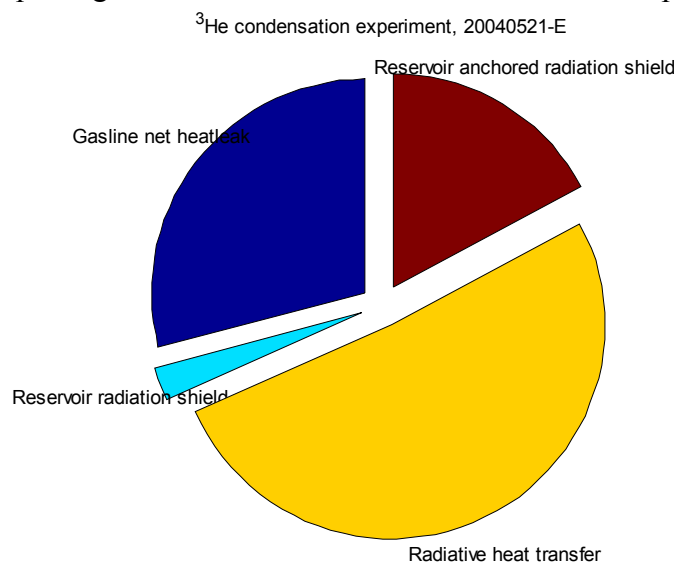


Figure 7.4: The pie chart above shows the relative sizes of the estimated heat leaks into the reservoir, with an assumed temperature of 82 K for the reservoir radiation shield. While the measurements from the ^3He condensation experiment indicated a temperature of 34 K, this measurement was not stable and also expected to increase as thermal equilibrium was achieved and the ^4He vapour flow decreased. Hence the older measurement from the preliminary set-up was used. Simulation '20040521-E' was used as a basis for the chart.

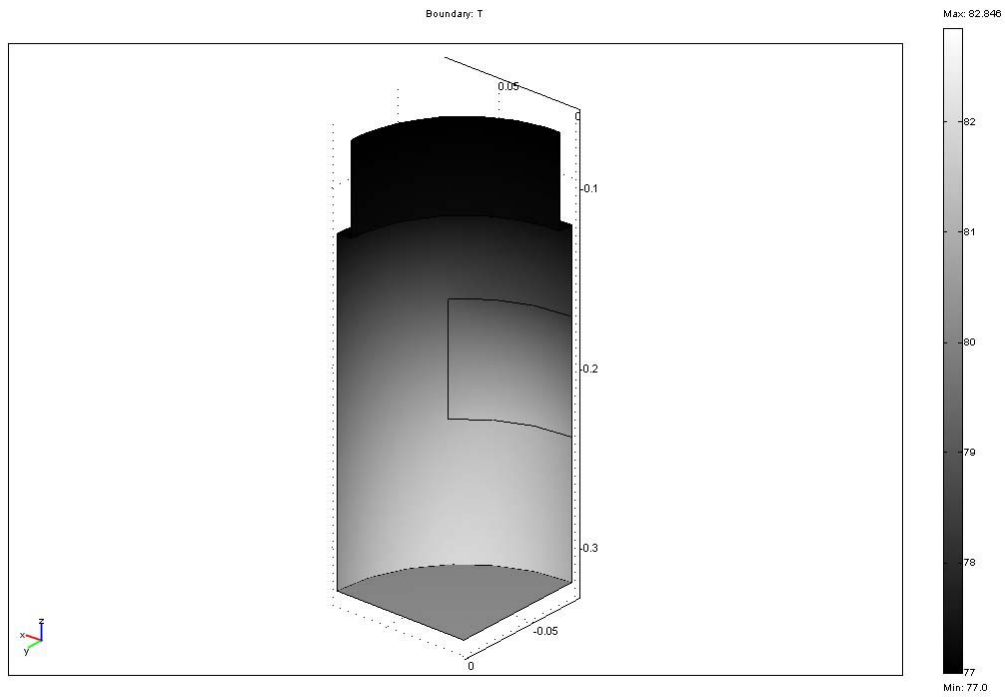


Figure 7.5: The radiation shield anchored to the liquid N₂ jacket dewar, in simulation ‘20040521-E’. An MLI blanket ϵ_{eff} of 0,06 and a thermal conductivity equal to that of OFHC Cu has been assumed. The spatial scale in the image is in meters, while the temperature scale is in degrees K. Note that the temperature scale has been truncated.

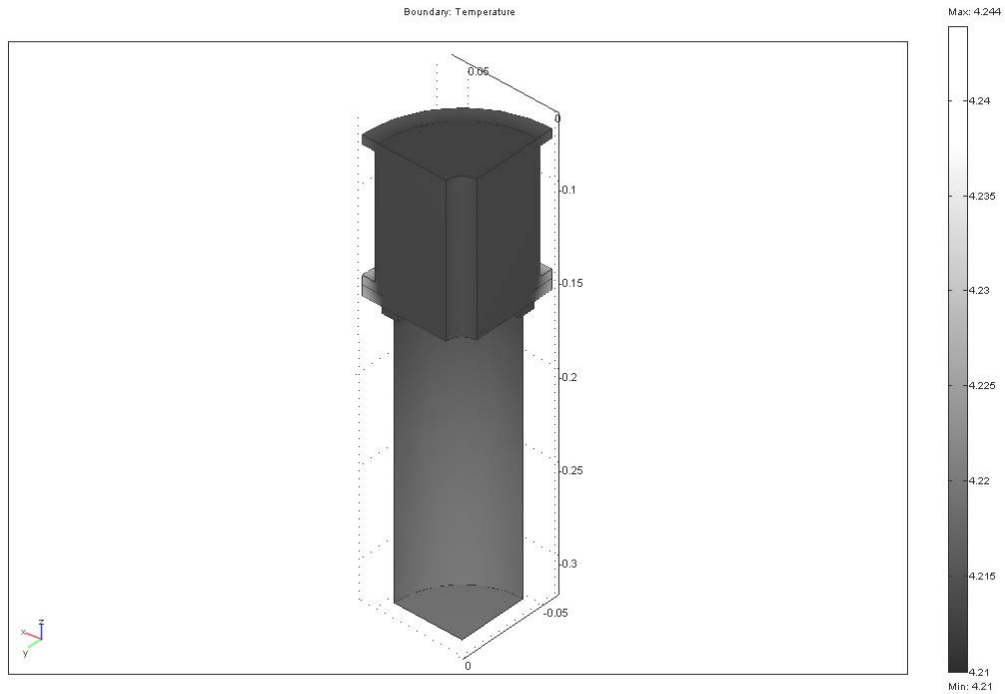


Figure 7.6: The lower portion of the reservoir with the radiation shield attached, assuming $\epsilon = 0,03$ for polished Cu and MLI $\epsilon_{\text{eff}} = 0,06$. Note that the hottest part is the reservoir lower steel flange. This is due to the flange emissivity being set to 0,28. In the experiment, as can be seen in Figure 5.5, the flange was not covered with MLI.

As can be seen in Figure 7.5, the simulated radiation shield temperature were 82,8 K for the liquid N₂ anchored shield. This corresponds exactly to the value acquired for the same Cu thermal conductivity and MLI ϵ_{eff} in the simulation the radiation shield in B. Nilsson's experiment. This is not surprising, since the only difference between the FEMLAB model used for simulating the radiation shield in B. Nilsson's experiment versus the shield in the ³He condensation model is the presence of the horizontal slit in the aluminium foil, something that did not noticeably affect the result.

Figure 7.6 shows the temperature distribution of the shield bolted to the reservoir, as calculated in simulation '20040521-E'. As was expected, the only two variables that affected the temperature distribution in the radiation shield were its thermal conductivity and emissivity. Since the temperature variations of both have been well documented (see section 3.3.1 and B.3) at different temperatures it was felt unnecessary to run multiple simulations, varying the two properties.

Simulation '20040521-E' showed a total radiative heat leak of 15,5 mW into the reservoir, of which 3,89 mW came from the reservoir anchored radiation shield. After estimating the remaining heat leaks as detailed in section 4.4.2, the total heat leak into the liquid ⁴He bath contained within the reservoir was calculated to 22,7 mW. Figure 7.4 shows the relative sizes of the contributing heat transfer processes.

The total heat leak into the LPC due to radiative heat transfer, the only heat transfer simulated using FEMLAB, was 31,4 μ W. Since the analysis of the data acquired, in section 6.1, had to utilise the methods and approximations detailed in the chapter on the physics model (section 4.4.2) in order to break down the total heat leak into its components, the 'simulated' values would be identical to the 'measured'.

7.2.2 Simulation validity

For the radiation shields, there is good agreement between the measured and simulated values for the liquid N₂ anchored shield; 84 K and 82,8 K respectively. Since the simulation is identical to the one performed for B. Nilsson's experiment, where the agreement with the measured value of 87 K was less than stellar, the improvement is entirely due to the different measured temperature. This may in turn be due to better thermal contact between the resistor and the shield, or it may be due to a more efficient application of the MLI blanket. The author is of the opinion that the latter is the more likely. An additional reason may be inadvertent contact between the two radiation shields.

As for the reservoir anchored radiation shield, the discrepancy between measured and simulated values is significant with $11,2 \pm 0,25$ K versus 4,224 K. This indicates, assuming there were no implementation or programming errors, that the simulation did not correspond to the real system.

An additional simulation '20040522-G' was run assuming far worse thermal conductivity along with higher shield emissivity. It was found that for the radiation shield to reach a maximum of 9 K, the thermal conductivity had to be 600 times less that of OFHC Cu and the emissivity be 0,3; ten times larger than the expected emissivity at 76 K. It would rather have been reasonable to expect a lower emissivity than 0,3 due to the decrease in temperature. Since it is unlikely that the real material properties are this far off the catalogued values, it is reasonable to assume that either the approximations made in calculating the radiative heat transfer is far off the mark or the system the data was measured from was not the system that was expected and modelled. Should it be the former, it is felt that the simulations of the liquid N₂ shield would have been more off the mark than they were. Should it be the latter, there may be three possible reasons for the discrepancy; bad thermal contact between diode and

shield, bad thermal contact between shield and reservoir and thermal contact between the shield and the liquid N₂ radiation shield.

Since the diode was attached on the inside of the radiation shield, which was not polished, there is an oxide layer between the diode and the thermally conducting copper. In addition, attachment was made only with tape since this had earlier proven sufficient for the resistors. These two factors both adversely affect the thermal contact between the diode and the shield, with the consequence that the heat generated by the measurement current can not be effectively carried off.

Further, as previously noted (see section 5.2.2) there might have been a good thermal contact between only part of the shield flange and the reservoir bottom, even though the bolts were tightened to improve the contact area. An attempt to include a contact resistance in the simulation failed, due to lack of time.

As for the last reason, the radiation shield bolted to the reservoir was made slightly too long. Consequently, there was only 1 mm leeway to a metal hood on the bottom of the liquid N₂ radiation shield. It is conceivable that, upon mounting the copper plates onto the liquid N₂ radiation shield, the Cu frame would have been distorted so that they were brought into contact. This could easily have increased the shield temperature to 11,2 K at the diode. This could then also explain the lower temperature of the liquid N₂ anchored radiation shield as compared to the measurement using the preliminary set-up. The author feels however, that the lower temperature may just as well be due to the different application of the MLI blanket.

As for heat leaks, the upper limit of 70 mW on the heat leak into the reservoir is not breached. On the contrary, the simulations seem to suggest that less than a fourth of that is possible. To make any conclusion regarding the validity of the simulation model solely based on this would however be rash. At most, it can be said that the simulated and the measured heat leaks are likely of the same order.

The assumption in the physics model that the rising helium vapour in the pumping pipe will carry off all heat conducted down along the wall is supported by the low-temperature, i.e. the non-steady-state, test. As Figure 6.1 show, the linear increase in the helium level indicates that neither the heat conduction nor the radiative heat transfer between the pumping tube walls play a part. It should however be noted that the flow of vapour is very large, so should a new, larger flow impedance be used instead of the present refill capillary the assumption may be false.

8 Conclusions

To recapture, the goals of this thesis project were:

1. To develop a simulation environment of the cryostat system at MAX-lab.
2. To build a cryostat prototype allowing condensation of ^3He .

The first goal has, depending on how one interprets it, been only partly achieved. The simulation models that have been developed cover only the cryostat volume enclosed by the vacuum chamber. In order to fully simulate the cryosystem performance, a model dealing with the convection heat transfer in the reservoir and pumping tube would have to be included. In addition, the performance of the new cryosystem design has been shown to be very dependant upon the fixed flow impedance between the reservoir and the low-pressure chamber. A simulation model that would assist in the design of such the impedance would have been most useful. As matters stand, these two things are possible future projects should the need arise.

On the positive side, the simulation model allowed identification of the major heat leaks in the new cryosystem and thus what parts of the cryosystem that need the most attention. In light of this, the somewhat mediocre agreement between actual cryosystem performance and simulated cryosystem performance is less important.

The second goal was not per se achieved, as no actual condensation of ^3He was obtained. This was however due to a cold leak in the ^3He gas line – the low temperatures necessary for condensation were easily achieved, albeit for a period of only ten minutes.

For MAX-lab, the partial fulfilment of the first goal is ‘good enough’. The priority for the Photonuclear research group is to obtain a cryosystem capable of sustaining a liquid ^3He target indefinitely, with refills of liquid ^4He coming periodically at least a day apart. From this point of view, knowing what to work on is more important than accurately predicting the thermal performance of the cryosystem. Also from this point of view, the ten minute period the cryosystem can keep ^3He condensed is not good enough and will have to be extended for any measurements on three nucleon forces to be feasible.

Appendix A: Simulation list

A.1 Original cryosystem simulations

20040428-F

Temperature data from measurements on the preliminary cryosystem setup utilised.
Liquid N₂ anchored shield is assumed to be made of OFHC Cu with an oxide layer.
All steel details are assumed to be made out of 316 Stainless steel, cleaned with chemicals.
MLI ϵ_{eff} set to 0,06 for all blankets.
The reservoir and target ϵ_{eff} was set to 0,50.

20040514-G

Temperature data from measurements on the preliminary cryosystem setup utilised.
Liquid N₂ anchored shield is assumed to be made of OFHC Cu with an oxide layer.
All steel details are assumed to be made out of 316 Stainless steel, cleaned with chemicals.
MLI ϵ_{eff} set to 0,06 for all blankets.
The reservoir and target ϵ_{eff} was set to 0,90.

20040514-H

Temperature data from measurements on the preliminary cryosystem setup utilised.
Liquid N₂ anchored shield is assumed to be made of Cu RRR=20 with an oxide layer.
All steel details are assumed to be made out of 316 Stainless steel, cleaned with chemicals.
MLI ϵ_{eff} set to 0,06 for all blankets.
The reservoir and target ϵ_{eff} was set to 0,50.

20040514-I

Temperature data from measurements on the preliminary cryosystem setup utilised.
Liquid N₂ anchored shield is assumed to be made of Cu RRR=20 with an oxide layer.
All steel details are assumed to be made out of 316 Stainless steel, cleaned with chemicals.
MLI ϵ_{eff} set to 0,03 for all blankets.
The reservoir and target ϵ_{eff} was set to 0,50.

20040514-J

Temperature data from measurements on the preliminary cryosystem setup utilised.
Liquid N₂ anchored shield is assumed to be made of Cu RRR=20 with an oxide layer.
All steel details are assumed to be made out of 316 Stainless steel, cleaned with chemicals.
MLI ϵ_{eff} set to 0,045 for all blankets.
The reservoir and target ϵ_{eff} was set to 0,50.

A.2 ³He condensation cryosystem simulations

20040506-C

Non-functional physics model.

Geometry model expanded through removal of one vertical symmetry plane.

Intended for inclusion of point sources representing diodes and capillaries.

20040521-E

Temperature data from ³He condensation experiment utilised.

Liquid N₂ anchored shield is assumed to be made of OFHC Cu with an oxide layer, while the reservoir anchored shield is assumed to be made of polished Cu RRR=20.

All steel details are assumed to be made out of 316 Stainless steel, cleaned with chemicals.

MLI ϵ_{eff} set to 0,06 for all blankets.

20040523-F

Temperature data from ³He condensation experiment utilised.

Liquid N₂ anchored shield is assumed to be made of Cu RRR=20 with an oxide layer, while the reservoir anchored shield is assumed to be made of polished Cu RRR=20.

All steel details are assumed to be made out of 316 Stainless steel, cleaned with chemicals.

MLI ϵ_{eff} set to 0,045 for all blankets.

20040523-G

Temperature data from ³He condensation experiment utilised.

Liquid N₂ anchored shield is assumed to be made of Cu RRR=20 with an oxide layer, while the reservoir anchored shield is assumed to be made of a material roughly equal to phosphor bronze in terms of thermal conductivity for temperatures below 10 K. This material is assumed to have an emissivity of 0,3.

All steel details are assumed to be made out of 316 Stainless steel, cleaned with chemicals.

MLI ϵ_{eff} set to 0,045 for all blankets.

Appendix B: Material properties

This appendix contains the material data utilised throughout the thesis project, as well as their source. First there will be short descriptions of a few select materials and their application at cryogenic temperatures. Then there will be comments on the use of MATLAB property functions in FEMLAB, followed by a table showing the material properties used throughout the simulations. For a list detailing the sources of material properties, see Appendix B.3.

B.1 Material descriptions

B.1.1 Liquid ^4He

Liquid ^4He will, once the temperature drops below the λ -point at 2,17 K in the ^4He phase diagram, undergo a phase transition where ‘normal phase’ ^4He is converted into ‘superfluid’ ^4He . These two fluid phases are normally referred to as He I and He II, respectively. Characteristic of He II is that it has a slew of unusual properties. For example, according to the two-fluid theoretical model of superfluid ^4He , part of the ^4He liquid will have zero viscosity and entropy; this is supported by experimental data. The bulk fluid will be observed to have extremely high heat conductivity and can be observed flowing upwards along walls.

To explain the unique properties of superfluids a great deal of knowledge in quantum mechanics is required; rather than attempt an explanation in this thesis, the author will only mention a few of the superfluid phenomenon of import to the thesis project and refer the reader to textbooks such as ‘Basic superfluids’ by A.M. Guenault [47] for a theoretical treatment of the subject.

Beside those properties mentioned above, a superfluid flow in a thin channel can be induced by a temperature gradient along the channel. This flow will go from low temperatures to high, in order to minimise the temperature gradient and equalise the temperatures at the ends of the channel. Unlike other flows, which are driven by a pressure difference, superfluid flows can thus be induced by temperature differences as well.

In addition, at the phase transition some bulk properties of liquid ^4He change. For flows through thin channels, fluid viscosity can be said to drop rapidly to zero below the transition provided the flow is not too large. Further, there is a spike in the specific heat capacity for constant pressure at the transition. Density however, is not affected much.

B.1.2 MLI and aluminised mylar

Aluminised mylar consists of a sheet of mylar plastic, roughly 6 μm , upon which an aluminium coating about 30 nm thick has been applied. The resulting film is light, mechanically resilient and easy to use as it doesn’t tear easily. Further it has a very low emissivity due to the aluminium coating. It has a high thermal conductivity along the film, also due to the aluminium coating, while the thermal conductivity normal to the film is far less due to the mylar backing. This difference in thermal conductivity is often of the order of 1000 times.

These properties make aluminised mylar a good choice for MLI (Multi-Layer Insulation) systems. This method of thermal radiation insulation relies on the use of multiple layers with high reflectance. Ideally, each layer would transfer heat to the next only radiatively and thus each layer would greatly decrease the amount of heat transfer through the MLI blanket. Realistically however, while convection and accommodation heat transfer can be almost

eliminated by a good enough vacuum, thermal conduction between layers is unavoidable as something must support them. In order to reduce this thermal conduction normal to the layers, additional layers of spacer material (silk or Dacron nets for example) are inserted between each reflecting layer. Care must be taken that actual physical contact between layers has as small an area and as low a thermal conductivity as possible, for a specific MLI blanket to achieve its optimal thermal performance.

The advantages with MLI blankets are that they are lightweight compared to alternatives such as polished metal plates and has the best performance of any radiative heat transfer isolation known. This has made them very popular in space applications, where they fit the dual requirements of low launch weight and good thermal isolation.

However, MLI has a few drawbacks. Blanket performance is unpredictable and the same blanket applied a second time under controlled conditions frequently performs differently than it did the first. Metal supports penetrating the blanket can act as thermal bridges between layers, effectively short-circuiting parts of the blanket. Blanket joints may also result in such short-circuiting, depending on how they are made. This also indicates the second drawback – proper assembly and handling of an MLI blanket is difficult.

B.1.3 Aluminium

Aluminium has high thermal conductivity and a low emissivity. However, both are slightly lower and higher, respectively, than for copper. The reason for using aluminium instead for cryogenic applications is that the emissivity of aluminium in the far IR-range does not worsen substantially with oxidation, in contrast with copper. The reason is that aluminium oxide is fairly transparent for thermal radiation [48], thus a thin oxide layer does not appreciably affect the emissivity.

Further, aluminium foil is cheap and plentiful as standard household foil usually suffices.

B.1.4 Copper

Pure copper has several advantageous properties at cryogenic temperatures from an engineering viewpoint. It has a very high thermal conductivity, which as an example makes it ideally suited for radiation heat shields as whatever heat is absorbed in them can quickly be carried away to a thermal sink or transferred to another medium in a heat exchanger. Further, commercial polished copper has a very low emissivity at $\epsilon = 0,03$ for 76 K [49] which is a requirement for radiation heat shields.

The problems with copper are that it has very high thermal conductivity and that polished Cu does not stay polished for long.

While the high thermal conductivity is generally considered an asset, inadvertent thermal contact between Cu details in a cryostat can introduce large heat leaks.

As for polished Cu surfaces, copper quickly oxidises. This covers a polished copper surface with copper oxide within a few weeks, increasing the emissivity to roughly $\epsilon = 0,6$ [50]. To avoid the necessity of repeatedly polishing copper heat shields it is common to apply a thin layer of gold, which like copper has a very low emissivity but famously does not oxidise.

OFHC Cu, or Oxygen-Free-High-Conductivity Cu, is commonly used in cryogenic applications due to its exceptionally high purity which grants it even higher thermal conductivity than traditional ‘pure’ copper.

B.1.5 Stainless steel

The advantage of stainless steel in cryogenic engineering is that it has low thermal conductivity while being mechanically resilient. It is therefore an ideal material for structural supports and tubing.

B.1.6 Lead

A useful property of lead is that it is superconducting at temperatures below the so-called critical temperature, which for lead is 7,2 K providing that no magnetic field is present. If there is a magnetic field present, the critical temperature will drop and should the magnetic field strength exceed a critical value lead will not go superconducting no matter the temperature.

Any material that is in its superconducting state will no longer have a contribution to its thermal conductivity from free electrons, since these have (to an overwhelming majority) formed Cooper pairs and will not easily change state. This allows a lead block between two reservoirs at differing temperatures but below 7,2 K to be used as a thermal switch with no moving parts. In order to operate the switch a magnetic field in excess of the critical field is applied, which causes the lead to revert to the normal state and to high thermal conductivity.

No leaden detail were used in either of the cryosystems, though they were discussed at a few points during development.

B.2 MATLAB property functions

At liquid helium temperatures, the variation of material properties with temperature is in most cases a factor necessary to include in any analysis. This is especially so for gases and liquids. Therefore the use of property functions such as $k(T)$ and $\rho(T)$ was necessary in the FEMLAB simulations. Some difficulties arose, since the vanilla property functions acquired from different sources, such as NIST, had to be adjusted for FEMLAB use. In order to allow a problem stated in FEMLAB to converge, the property functions needed to be continuous, finite and able to return values even for negative temperatures. Additionally, FEMLAB required a MATLAB function for the derivatives of each property function.

This adjustment was achieved through mirroring the, primarily logarithmic, functions with respect to $T = 0$. In the cases where the original functions did not remain finite at $T = 0$, they were truncated to their stated lower valid limit. The mirrored and the original function were then connected by a polynomial matched to the first and ‘zeroth’ derivatives of the original and the mirrored function. I.e., the continuity of the property functions and their derivatives was ensured.

A problem during the thesis project was that while the bulk properties of a very large range of materials are well-known above 300 K, there is a dearth of information on the behaviour of different materials at cryogenic temperatures.

Material	ρ [kg m ⁻³]	c_p [J kg ⁻¹]	μ [Pa s ⁻¹]	k [W m ⁻¹ K ⁻¹]	$\epsilon(293 < T)$	$\epsilon(77 < T < 90)$	$\epsilon(T < 4.215)$
304L Stainless steel	7850	Cp_304L_Steel.m	-	k_304L_Steel.m	0,28	0,28	0,28
316 Stainless steel	7850	x	-	k_316_Steel.m	0,28	0,28	0,28
Cu RRR=20, polished	8700	x	-	α :k_OFHC_Cu.m	x	0,03	0,03
Cu RRR=20, oxidised	8700	x	-	α :k_OFHC_Cu.m	0,78	0,6	0,6
OFHC Cu, polished	8700	Cp_OFHC_Cu.m	-	k_OFHC_Cu.m	x	0,03	0,03
OFHC Cu, oxidised	8700	Cp_OFHC_Cu.m	-	k_OFHC_Cu.m	0,78	0,6	0,6
1100 aluminium	x	x	-	k_1100_Aluminium.m	x	0,04	x
QT36 phosphor bronze wire	x	x	-	k_QT36_wire.m	x	x	x
Kapton MT film	x	x	-	k_MT_Kapton.m	x	x	x
Kapton H film	x	x	-	k_H_Kapton.m	x	x	x
Liquid ⁴ He	x	x	x	x	x	x	1
⁴ He gas	rho 4He_gas.m	Cp 4He_gas.m	mu 4He_gas.m	k 4He_gas.m	x	x	x

Table 8.1: A list of what property values or MATLAB functions were utilised in the simulations for different materials. Where a value has been assumed, values are in italics. Note that, especially in the case of the assumed emissivities, the values are worst-case. The α factor present in the Cu RRR=20 thermal conductivities varies depending on the temperature range. For $T < 10$ K, $\alpha \approx 1/6$ while for $77 \text{ K} < T < 90 \text{ K}$ $\alpha \approx 1/2$. An ‘x’ indicates that this property was not utilised in the simulations, while a ‘-’ indicates that this property was not applicable to the material in question.

B.3 Material data sources

Emittance data:

Electro Optical Industries, Inc. URL: http://www.electro-optical.com/bb_rad/emissivity/matlemisivty.htm (2004-05-16)

C. Bradkte, *A New Frozen-Spin Target for the Measurement of the Helicity Asymmetry of the Total Photoabsorption Cross-Section*, Physikalisches Institut, Universität Bonn, p. 49 (2000)

M. M. Fulk, M. M. Reynolds, *Emissivities of Metallic Surfaces at 76°K*, Journal of Applied Physics, vol. 28, p. 1464-1467 (1957)

M. F. Modest, *Radiative heat transfer 2nd Edition*, Academic press (2003), ISBN 0-12-503163-7

Thermal conductivity data:

D.J. Benford, T.J. Powers, S.H. Moseley, *Thermal conductivity of Kapton tape*, Cryogenics 39 (1999) 93-95

Handbook of Cryogenic Engineering, Taylor & Francis (1998), ISBN 1-56032-332-9

NIST Cryogenic Technologies Group, URL: <http://cryogenics.nist.gov> (2004-05-16)

Specific heat capacity data:

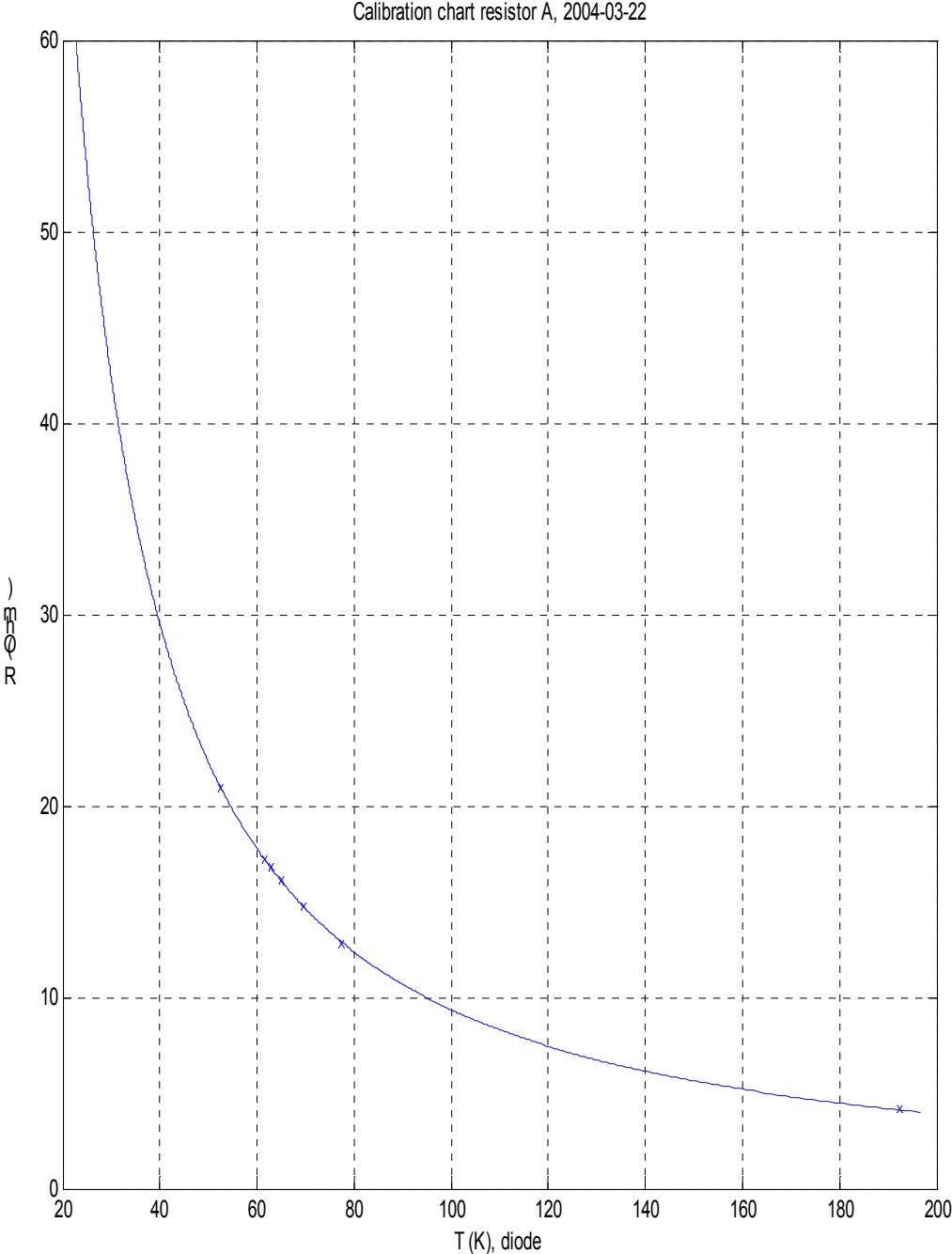
Handbook of Cryogenic Engineering, Taylor & Francis (1998), ISBN 1-56032-332-9

NIST Cryogenic Technologies Group, URL: <http://cryogenics.nist.gov> (2004-05-16)

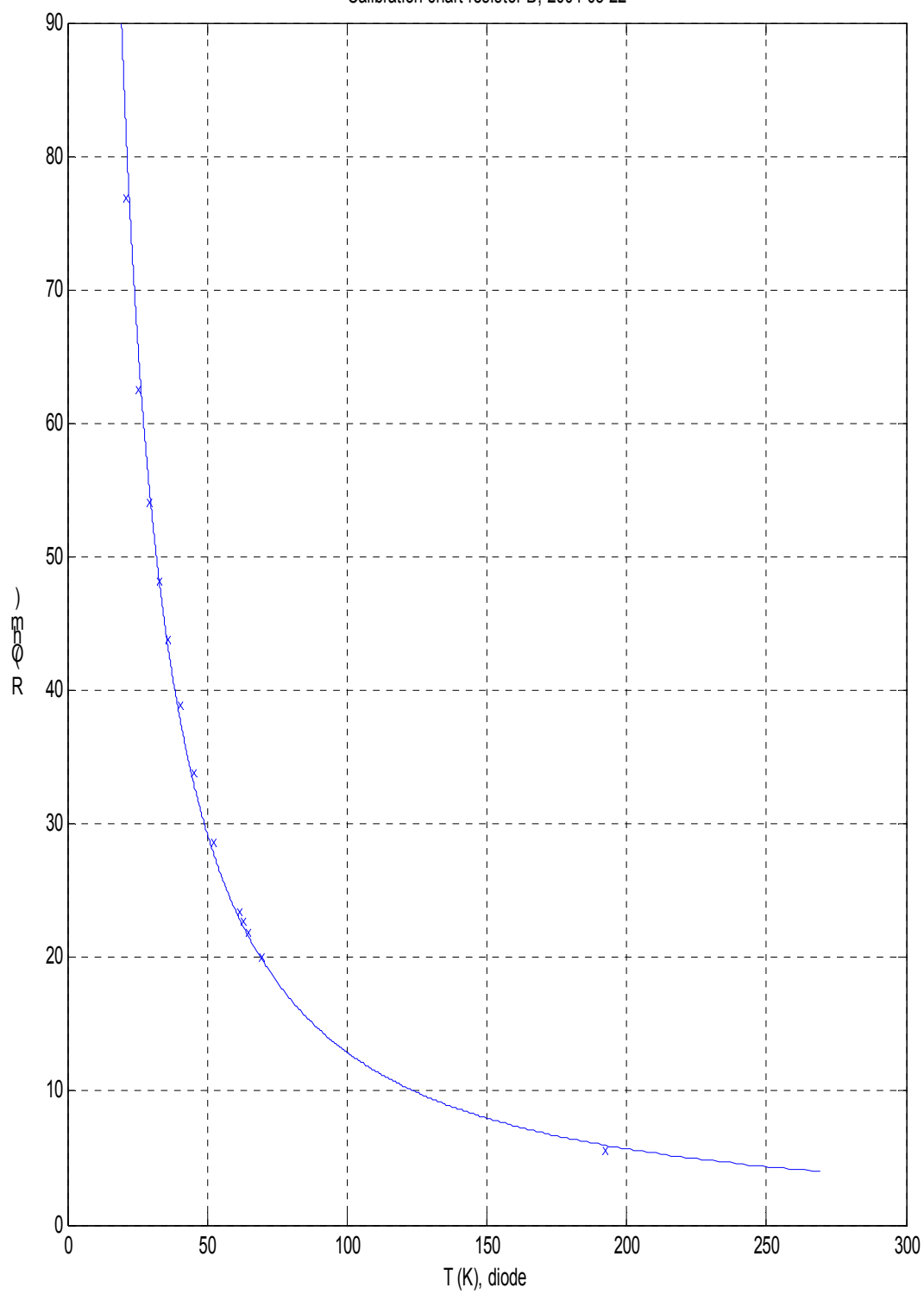
⁴He data:

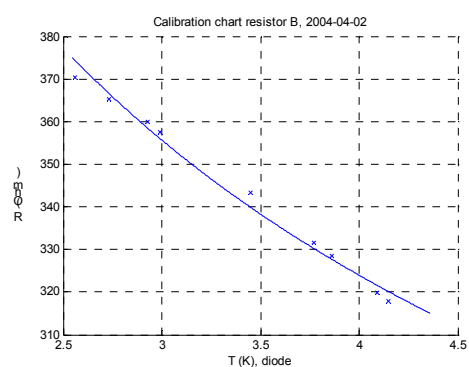
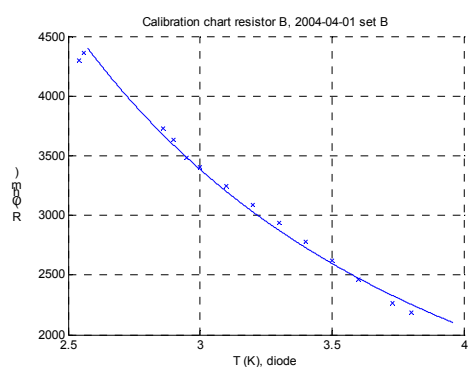
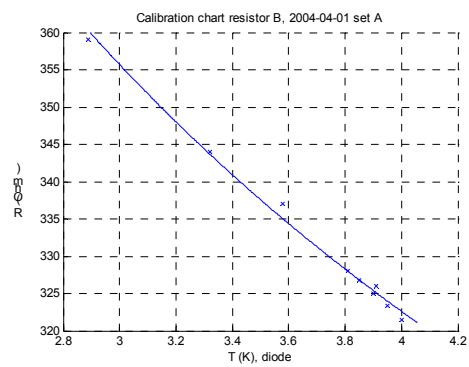
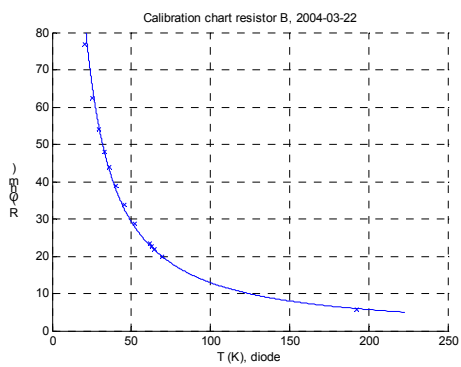
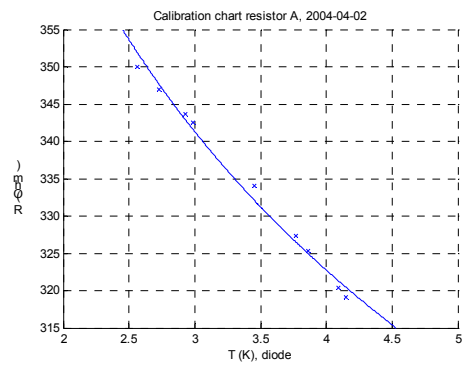
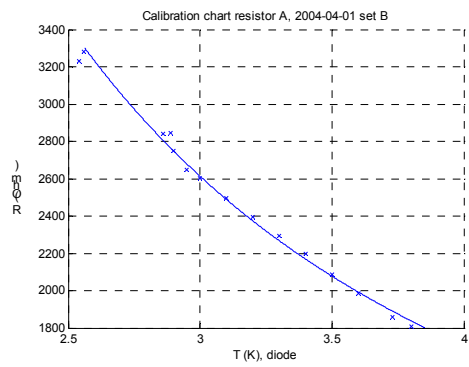
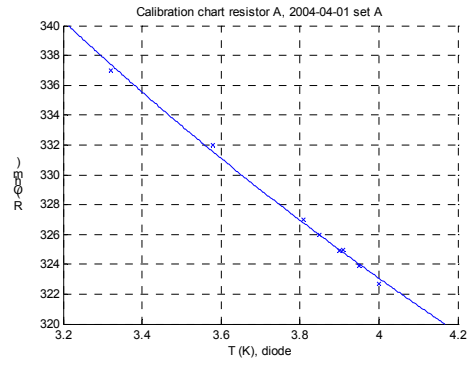
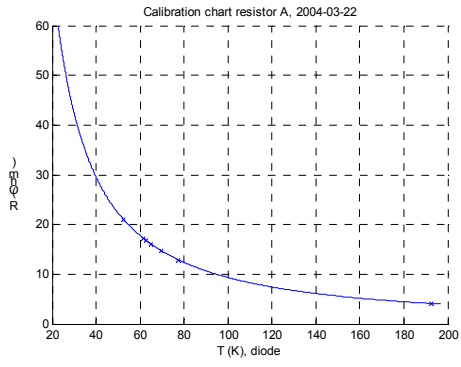
Handbook of Cryogenic Engineering, Taylor & Francis (1998), ISBN 1-56032-332-9

Appendix C: Calibration charts



Calibration chart resistor B, 2004-03-22





List of abbreviations

LPC:	Low Pressure Chamber
MLI:	MultiLayer Insulation
PDE:	Partial Differential Equation
VAT:	Value Added Tax

List of variables

- α = Absorptance, absorptivity
 α = Accommodation coefficient
 γ = Ratio of specific heats (c_p/c_v)
 ε = Emittance, emissivity
 η = Viscosity [Pa s]
 ρ = Density [kg m^{-3}]
 ρ = Reflectance
 ρ^d = Diffuse reflectance, diffuse reflectivity
 ρ^s = Specular reflectance, specular reflectivity
 σ_{dc} = Electrical direct current conductivity [$\Omega^{-1} \text{m}^{-1}$]
 τ = Transmittance, transmittivity
 A = Area [m^2]
 A = Mass number
 c = Specific heat capacity [$\text{J kg}^{-1} \text{K}^{-1}$]
 c_p = Specific heat capacity under constant pressure [$\text{J kg}^{-1} \text{K}^{-1}$]
 E_b = Emissive power for a blackbody [W]
 F_{i-j}^s = Specular view factor
 h = Convection heat transfer coefficient [$\text{W m}^{-2} \text{K}^{-1}$]
 k = Thermal conductivity [$\text{W m}^{-1} \text{K}^{-1}$]
 I = Electrical current [A]
 I_e = Electron beam current [A]
 \dot{M} = Mass flow [kg s^{-1}]
 M = Molecular weight [kg mol^{-1}]
 N_e = Number of electrons per unit time entering radiator foil [s^{-1}]
 n = Index of refraction
 Δp = Pressure difference [Pa]
 P = Power [W]
 P_e = Electron beam power [W]
 P_γ = Photon beam power [W]
 $P_{max\ deposited}$ = Maximum power deposited in a target by a photon beam [W]
 R = Radius [m]
 R = Universal gas constant [$\text{J mol}^{-1} \text{K}^{-1}$]
 q = Heat flux [W m^{-2}]
 q_0 = Heat source [W m^{-3}]
 q_{in} = Radiative heat flux into a surface [W m^{-2}]
 q_{out} = Radiative heat flux out from a surface [W m^{-2}]
 T = Temperature [K]
 T_b = Fluid bulk temperature [K]
 T_w = Wall temperature [K]
 U = Electrical voltage [V]
 \dot{V} = Volume flow [$\text{m}^3 \text{s}^{-1}$]
 X_0 = Radiation length [kg m^{-2}]
 Z = Atomic number
 Z = Flow impedance [m^{-3}]

Literature list

Handbook of Cryogenic Engineering, Taylor & Francis (1998), ISBN 1-56032-332-9

C. Bradkte, *A New Frozen-Spin Target for the Measurement of the Helicity Asymmetry of the Total Photoabsorption Cross-Section*, Physikalisches Institut, Universität Bonn (2000)

A. Christ, H. J. Gassen, G. Nöldeke, T. Reichelt, H. Stanek, *A liquid ^3He target for scattering experiments*, Nuclear instruments and methods 152 p.367-369; North-Holland publishing co. (1978)
(Physikalisches Institut, Universität Bonn, D5300 Bonn, Germany)

L.E. DeLong, O.G. Symko, J.C. Wheatley, *Continuously operating ^4He evaporation refrigerator*, The review of scientific instruments 42 p.147-150, The American institute of physics (Jan. 1971)

M. M. Fulk, M. M. Reynolds, *Emissivities of Metallic Surfaces at 76°K*, Journal of Applied Physics, vol. 28, p. 1464-1467 (1957)

M. Gauthier, E. J. A. Varoquaux, *Flow impedance construction for liquid helium continuous refrigerators*, Cryogenics, p. 272-273, (May 1973)

A. M. Guenault, *Basic superfluids*, Taylor & Francis (2002), ISBN 0748408924

[K. Hagiwara et al.](http://pdg.lbl.gov), *Review of Particle Physics*, Phys. Rev. D vol. 66, 010001 (2002), URL: <http://pdg.lbl.gov> (cited 2004-05-16)

D.K. Hasell, R. Abegg, B.T. Murdoch, W.T.H. van Oers, H. Postma, J. Soukup, *A liquid ^3He target system for use at intermediate energies*, Nuclear instruments and methods 189 p.341-346, North-Holland publishing co. (1981)

J. R. Hook, H. E. Hall, *Solid state physics 2nd Edition*, John Wiley & Sons Ltd (2001), ISBN 0-471-92805-4

S. Kato, K. Kobayashi, K. Maruyama, H. Okuno, O. Konno, T. Suda, T. Maki, H. Asami, T. Koizumi, *A new type of liquid- ^3He target system using small mechanical refrigerators*, Nuclear instruments and methods in physics research A307 p.213-219, North-Holland (1991)

G. Lawes, G.M. Zassenhaus, S. Koch, E.N. Smith, J.D. Reppy, J.M. Parpia, *Reduction of vibrational noise from continuously filled 1K pots*, Review of scientific instruments vol.69 #12 p.4176-4178, The American institute of physics (Dec. 1998)

H.C. Meijer, H. Postma, W.B. Bloem, *Test and analysis of a liquid ^3He target for intermediate energy physics experiments*, Nuclear instruments and methods in physics research A234 p.421-425, North-Holland (1985), Amsterdam

M. F. Modest, *Radiative heat transfer 2nd Edition*, Academic press (2003), ISBN 0-12-503163-7

B. Nilsson, *High-Resolution Measurement of the $4\text{He}(\gamma,n)$ Reaction in the Giant Resonance Region*, Ph. D. thesis, Department of Physics, Lund University (2003), ISBN 91-628-5615-4

H. Postma, J. P. Boogaard, P. H. M. Keizer, L. Prins, P. K. A. De Witt Huberts, *A high power liquid $^3,^4\text{He}$ target system for electron scattering experiments*, Nuclear instruments and methods in physics research 219 p.292-296; North-Holland (1984), Amsterdam

A. Raccanelli, L.A. Reichertz, E. Kreysa, *Eliminating the vibrational noise in continuously filled 1K pots*, Cryogenics 41 p.763-766, Elsevier Science Ltd. (2001)

G. Sparr, A. Sparr, *Kontinuerliga system*, Studentlitteratur (1999), ISBN 91-44-01355-8

List of references

- [1] W. Glöckle, J. Golak, R. Skibiński, H. Witala, A. Nogga, *Photodisintegration of ^3He : Search for Three-Nucleon Force Effects in PROCEEDINGS of the Second MAX-lab Workshop on the Nuclear Physics Program with Real Photons below 250 MeV*, Lund University (May 2002)
- [2] B. Nilsson, *High-Resolution Measurement of the $^4\text{He}(\gamma, n)$ Reaction in the Giant Resonance Region*, Dep. of Physics, Lund University (2003), ISBN 91-628-5615-4
- [3] T. Glebe, *Comptonstreuung an ^4He im Quasideuteronbereich*, Thesis, Georg-August-Universität, Göttingen (1996)
- [4] S. Proff, *Elastische Photonsteuerung an ^4He und ^{16}O im Quasideuteronbereich*, Thesis, Georg-August-Universität, Göttingen (1998)
- [5] B. Nilsson, *High-Resolution Measurement of the $^4\text{He}(\gamma, n)$ Reaction in the Giant Resonance Region*, Dep. of Physics, Lund University, p. 97, 152 (2003), ISBN 91-628-5615-4
- [6] Communication, Spectra Gases GmbH (2003-09-25)
- [7] H. C. Meijer, H. Postma, *Test and analysis of a liquid ^3He target for intermediate energy physics experiments*, Nuclear Instruments and Methods in Physics Research A234, p. 422 (1985)
- [8] Private communication, H. Dutz, Polarised Target Group, Universität Bonn
- [9] A. Raccanelli, L. A. Reichertz, E. Kreysa, *Eliminating the vibrational noise in continuously filled 1K pots*, Cryogenics 41, 763-766 (2001)
- [10] M. Gauthier, E. J. A. Varoquaux, *Flow impedance construction for liquid helium continuous refrigerators*, Cryogenics, p. 272-273, (May 1973)
- [11] L. E. DeLong, O. G. Symko, J. C. Wheatley, *Continuously operating ^4He evaporation refrigerator*, The review of scientific instruments, vol. 42 #1, p. 147 (Jan 1971)
- [12] M. Gauthier, E. J. A. Varoquaux, *Flow impedance construction for liquid helium continuous refrigerators*, Cryogenics, p. 272-273, (May 1973)
- [13] M. Gauthier, E. J. A. Varoquaux, *Flow impedance construction for liquid helium continuous refrigerators*, Cryogenics, p. 272, (May 1973)
- [14] *Handbook of Cryogenic Engineering*, Taylor & Francis, p.164 (1998), ISBN 1-56032-332-9
- [15] G. Sparr, A. Sparr, *Kontinuerliga system*, Studentlitteratur, p.8 (1999), ISBN 91-44-01355-8
- [16] MATLAB v6.5 rel. 13 SP 1 help file (2004-05-16)
- [17] *Handbook of Cryogenic Engineering*, Taylor & Francis, p.164-178 (1998), ISBN 1-56032-332-9
- [18] M. F. Modest, *Radiative heat transfer 2nd Edition*, Academic press, p. 10 (2003), ISBN 0-12-503163-7
- [19] M. F. Modest, *Radiative heat transfer 2nd Edition*, Academic press, p. 21 (2003), ISBN 0-12-503163-7
- [20] M. F. Modest, *Radiative heat transfer 2nd Edition*, Academic press, p. 30 (2003), ISBN 0-12-503163-7
- [21] M. F. Modest, *Radiative heat transfer 2nd Edition*, Academic press, p. 188 (2003), ISBN 0-12-503163-7
- [22] M. F. Modest, *Radiative heat transfer 2nd Edition*, Academic press, ch. 6.3 (2003), ISBN 0-12-503163-7
- [23] M. F. Modest, *Radiative heat transfer 2nd Edition*, Academic press, p. 201 (2003), ISBN 0-12-503163-7
- [24] M. F. Modest, *Radiative heat transfer 2nd Edition*, Academic press, p. 202-203 (2003), ISBN 0-12-503163-7
- [25] M. F. Modest, *Radiative heat transfer 2nd Edition*, Academic press, p. 80 (2003), ISBN 0-12-503163-7
- [26] J. R. Hook, H. E. Hall, *Solid state physics 2nd Edition*, John Wiley & Sons Ltd, ch. 3.3.4 (2001), ISBN 0-471-92805-4
- [27] *Handbook of Cryogenic Engineering*, Taylor & Francis, p.178 (1998), ISBN 1-56032-332-9
- [28] *Handbook of Cryogenic Engineering*, Taylor & Francis (1998), ISBN 1-56032-332-9
- [29] B. Nilsson, *High-Resolution Measurement of the $^4\text{He}(\gamma, n)$ Reaction in the Giant Resonance Region*, Dep. of Physics, Lund University, Appendix B (2003), ISBN 91-628-5615-4
- [30] B. Nilsson, *High-Resolution Measurement of the $^4\text{He}(\gamma, n)$ Reaction in the Giant Resonance Region*, Dep. of Physics, Lund University, p. 156 (2003), ISBN 91-628-5615-4
- [31] H. C. Meijer, H. Postma, *Test and analysis of a liquid ^3He target for intermediate energy physics experiments*, Nuclear Instruments and Methods in Physics Research A234, p. 421-425 (1985)
- [32] [K. Hagiwara et al.](http://pdg.lbl.gov), *Review of Particle Physics*, Phys. Rev. D vol. 66, 010001 (2002), URL: <http://pdg.lbl.gov> (cited 2004-05-16)
- [33] [K. Hagiwara et al.](http://pdg.lbl.gov), *Review of Particle Physics*, Phys. Rev. D vol. 66, 010001 (2002), URL: <http://pdg.lbl.gov> (cited 2004-05-16)
- [34] B. Nilsson, *High-Resolution Measurement of the $^4\text{He}(\gamma, n)$ Reaction in the Giant Resonance Region*, Dep. of Physics, Lund University (2003), ISBN 91-628-5615-4
- [35] Electro Optical Industries, Inc. URL: http://www.electro-optical.com/bb_rad/emissivity/matlemisivty.htm (cited 2004-05-16)

-
- [36] B. Nilsson, *High-Resolution Measurement of the $^4\text{He}(\gamma, n)$ Reaction in the Giant Resonance Region*, Dep. of Physics, Lund University, p. 175 (2003), ISBN 91-628-5615-4
- [37] LakeShore Cryotronics, URL: <http://www.lakeshore.com/temp/acc/am.html> (cited 2004-05-15)
- [38] C. R. Nave, *HyperPhysics*, Department of Physics and Astronomy, Georgia State University (2003), URL: <http://hyperphysics.phy-astr.gsu.edu/hbase/solids/scond.html> (cited 2004-05-21)
- [39] *Handbook of Cryogenic Engineering*, Taylor & Francis, ch. 3-2-2 (1998), ISBN 1-56032-332-9
- [40] A. Raccanelli, L. A. Reichertz, E. Kreysa, *Eliminating the vibrational noise in continuously filled 1K pots*, *Cryogenics* 41, 763-766 (2001)
- [41] B. Nilsson, *High-Resolution Measurement of the $^4\text{He}(\gamma, n)$ Reaction in the Giant Resonance Region*, Dep. of Physics, Lund University, p. 191 (2003), ISBN 91-628-5615-4
- [42] B. Nilsson, *High-Resolution Measurement of the $^4\text{He}(\gamma, n)$ Reaction in the Giant Resonance Region*, Dep. of Physics, Lund University, p. 175 (2003), ISBN 91-628-5615-4
- [43] B. Nilsson, *High-Resolution Measurement of the $^4\text{He}(\gamma, n)$ Reaction in the Giant Resonance Region*, Dep. of Physics, Lund University, p. 191 (2003), ISBN 91-628-5615-4
- [44] B. Nilsson, *High-Resolution Measurement of the $^4\text{He}(\gamma, n)$ Reaction in the Giant Resonance Region*, Dep. of Physics, Lund University, p. 175-176 (2003), ISBN 91-628-5615-4
- [45] Private communication, K. Hansen, Photonuclear research group, MAXLAB
- [46] *Handbook of Cryogenic Engineering*, Taylor & Francis (1998), ISBN 1-56032-332-9
- [47] A. M. Guenault, *Basic superfluids*, Taylor & Francis (2002), ISBN 0748408924
- [48] C. Bradkte, *A New Frozen-Spin Target for the Measurement of the Helicity Asymmetry of the Total Photoabsorption Cross-Section*, Physikalisches Institut, Universität Bonn, p. 49 (2000)
- [49] M. M. Fulk, M. M. Reynolds, *Emissivities of Metallic Surfaces at 76°K*, *Journal of Applied Physics*, vol. 28, p. 1466 (1957)
- [50] C. Bradkte, *A New Frozen-Spin Target for the Measurement of the Helicity Asymmetry of the Total Photoabsorption Cross-Section*, Physikalisches Institut, Universität Bonn, p. 49 (2000)